



ADVANCED ELECTROMAGNETIC METHODS FOR AEROSPACE VEHICLES

Semiannual Progress Report
(January 1 - June 30, 1992)

by
Constantine A. Balanis
Weimin Sun
El-Budawy El-Sharawy
James T. Aberle
Craig R. Birtcher
Jian Peng
Panayiotis A. Tirkas

LANGLEY
GRANT
N-32-CR
115129
P.63

N92-31156

Unclass

G3/32 0115129

Prepared by

Telecommunications Research Center
College of Engineering and Applied Science
Arizona State University
Tempe, AZ 85287-7206

Sponsored by

Grant No. NAG-1-1082
National Aeronautics and Space Administration
Langley Research Center
Hampton, VA 23665

(NASA-CR-190650) ADVANCED
ELECTROMAGNETIC METHODS FOR
AEROSPACE VEHICLES Semiannual
Progress Report, 1 Jan. - 30 Jun.
1992 (Arizona State Univ.) 63 p



Contents

I. INTRODUCTION	1
II. COMPOSITE MATERIALS	3
A. Introduction	3
B. RCS of Low Conductivity Composite Materials	4
C. Electromagnetic Penetration through Composite Panels	6
D. Interaction of EM Waves With a Stratified Composite Plate	8
III. ANTENNA TECHNOLOGY	41
A. Introduction	41
B. Stacked Microstrip Patch Antennas	41
C. Cavity-Backed Microstrip Patch Antennas	42
D. Varactor-Tuned Microstrip Patch Antennas	43
E. Ferrite-Controlled Cavity-Backed Slot Radiators	45
F. Future Work	49

I. INTRODUCTION

The Advanced Helicopter Electromagnetics (AHE) Industrial Associates Program continues its research on variety of main topics identified and recommended by the Advisory Task Force of the program. The research activities center on issues that advance technology related to helicopter electromagnetics. While most of the topics are a continuation of previous works, special effort has been focused on some of the areas due to recommendations from the last annual conference held at Arizona State University on October 23-24, 1991 and the biannual meeting of 1992 held at the Naval Air Warfare Center on May 13-14, 1992. The main topics addressed in this report are:

- Composite Materials
- Antenna Technology

The area of Composite Materials continues getting special attention in this period. The research has focused on:

- a. Measurements of the electrical properties of low-conductivity materials
- b. Modeling of material discontinuity and their effects on the scattering patterns (RCS)
- c. Preliminary analysis on interaction of electromagnetic fields with multilayered graphite fiberglass plates
- d. FDTD modeling of fields penetration through composite panels of a helicopter.

In previous research, our work on RCS and radiation pattern predictions was primarily limited to high conductivity materials which make little difference from perfect electric conductors. Considering that low conductivity materials are frequently used in modern aircraft industry, we have investigated the effects of those low conductivity materials on RCS of complex structures including conducting and composite materials. The spectral domain Green's function approach has been employed to model the composite by surface impedance, which in turn is coupled into the NEC code for pattern predictions. Some of the results are reported in this period. This report

also provides new measurement results on GDS composite material that we believe to be more accurate.

In light of the anisotropic property of a graphite fiberglass composite, basic analysis has been performed on the interaction of EM waves with an anisotropic multi-layered composite. The analysis is aimed to lay the basis for the introduction of anisotropic surface impedance. From the preliminary study, it is found that low frequency fields may penetrate through multi-layered composites depending on the number of layers and the fiber orientations.

As a follow-up, the shielding problems in a helicopter were examined further by using FD-TD method when some of the helicopter panels were replaced with composite materials.

In the area of Antenna Technology, significant progress has been made in investigations of different antenna elements such as stacked microstrips, cavity-backed microstrips, varactor-tuned microstrip patches and ferrite-loaded cavity-backed slots. These novel microstrip antenna concepts show some attractive features overcoming certain intrinsic short-comings of conventional microstrip antennas.

In particular, a two-dimensional analytical model of a magnetically-tuneable cavity-backed slot antenna is introduced in this report with specific intent of analyzing the scattering characteristics and the tuning capabilities of such an antenna at VHF and UHF frequencies. This analysis is hoped to demonstrate the tangibility of such an antenna and to bring a substantial amount of insight into the specific design considerations.

II. COMPOSITE MATERIALS

A. Introduction

The progress in the area of Composite Materials is significant and diverse. The major achievements are represented by the RCS prediction of low conductive composites, also EM wave penetration through composite panels into a helicopter, and analysis of EM wave interaction with anisotropic composite plates.

Since low conductivity materials are used frequently in modern helicopter platforms, it is necessary to study the effects of these materials on RCS of complex structures that include several types of conducting, semi-conducting and nonconducting materials. In this report, we investigate the RCS patterns of low conductivity composite materials including modeling the discontinuities between these materials and PEC. RCS comparisons were initially made because the effects of materials and material discontinuities are usually more evident in scattering patterns than they are in antenna patterns.

To illustrate the capabilities and potentials of the FDTD method to electromagnetic penetration and interaction problems on complex airframes, the perfectly conducting NASA helicopter airframe is replaced by a helicopter structure that is made of conducting and composite materials. The composite materials (fiberglass and teflon) used to replace some of the helicopter panels are typical samples of materials being used in the construction of modern helicopter airframes. The helicopter is then exposed to a plane wave and the electromagnetic fields penetrating the structure were computed using the FDTD method. The solution of the problem reveals the insight into wave penetration and interaction with on-board structures where vulnerable electronic equipment is housed.

Furthermore, in this report we also present an analytical formulation and numerical program for systematic prediction of EM wave reflection from and transmission through composite plates involving stratified anisotropic graphite-epoxy fiber sheets. Various numerical simulation results of the reflection and the transmission characteristics of stratified composites versus frequency are reported. A significant penetration of an electromagnetic wave through a composite plate at a low frequency range has been revealed by the numerical results. The strong dependency of the reflection and the transmission characteristics of a composite plate on the orientation of the fibers

composing the plate can be observed.

B. RCS of Low Conductivity Composite Materials

1. Introduction

In our previous reports we presented theory and measurements of:

- a. Antenna and RCS patterns on composite materials of high conductivity such as graphite epoxy and fiberglass with screens near the surface.
- b. Antenna patterns on composite materials of low conductivity including microwave absorbers.

In the above cases, the surface impedance of the composite material is evaluated using a spectral domain Green's functions approach and utilized to model the structure under investigation as a wire grid. The pattern of the structure is then computed using the wire grid option of NEC code. Monopole antennas on both high and low conductivity materials have been built and tested. Good agreement between predictions and measurements of radiation patterns of these antennas have been observed.

So far our work on RCS of composite materials has been limited to high conductivity materials. The RCS patterns of structures made of high conductivity materials were very similar to those made of perfect electric conductors (PEC). In this report, we investigate the RCS patterns of low conductivity composite materials including modeling the discontinuities between composites and PECs.

2. Theory and measurements

It has been shown in our previous reports that the surface impedance Z_s of a two-layer medium including a layer of composite material (Figure 1a), can be written as

$$\bar{\bar{Z}}_s = (\bar{\bar{T}}_E + \bar{\bar{Z}}_T \bar{\bar{G}}_s)(\bar{\bar{Y}}_T + \bar{\bar{T}}_J \bar{\bar{G}}_s)^{-1} \quad (1)$$

$$\bar{\bar{G}}_s = \bar{\bar{T}}_{LJ} \bar{\bar{Z}}_{LT}^{-1}$$

where $\bar{\bar{Z}}_T$, $\bar{\bar{Y}}_T$, $\bar{\bar{T}}_E$, $\bar{\bar{T}}_J$ are the transmission matrices of the composite material and the subscript L denotes the medium below the composite material. At the limit when the thickness d of the bottom layer equal zero, the surface impedance becomes

$$\bar{\bar{Z}}_s = \bar{\bar{Z}}_T \bar{\bar{T}}_J^{-1} \quad (2)$$

To verify our theory, a 4.0"x2.7"x0.06" aluminum plate was partially covered by a layer microwave absorber as shown in Figure 2 and the RCS pattern of this structure was measured at 4 GHz (the lowest operating frequency of our anechoic chamber at the time of the measurements). The dimensions of the absorber were 2.0"x2.7"x0.03" (half the size of the plate) The electric properties of the absorber material were measured at X band (8.2-12.4 GHz) using the waveguide technique and are shown in Figures 3-6. The measured properties were then interpolated to $\epsilon_r=14.9-j0.1$, $\mu_r=2.0-j1.6$ at 4 GHz (RCS measurement frequency). There has not been any other accurate technique, available to us, to directly measure the absorber material properties at 4 GHz. The surface impedance was computed using the above theory for different angles of incidence. Very small variations of the surface impedance versus the angle of incidence have been predicted ($41.8 - j48.2\Omega \pm 10\%$). Using this computed value of the surface impedance, the NEC code was used to model and compute the RCS pattern of the structure shown in Figure 2. The results are shown in Figure 7. Note that, since the aluminum plate in this was relatively thick (0.06"), it was supposed to model the plate by two grid layers at the surface of the plate. However, to save CPU time and computer memory, only one PEC grid at the center was used to model the aluminum plate. The measured pattern and the calculated pattern using our theory are in good agreement. The absorber has a noticeable effect on pattern symmetry as well as on the intensity of the main beams. The main beam on the absorber side was about 3 dB less than the PEC side.

3. Conclusion and future work

The effects of low conductivity composite materials on the RCS patterns of antennas have been analyzed and presented. The code has been validated by computing the surface impedance comparing predicted patterns of a plate partially covered with a microwave absorber material to measure-

ments. Presently, we are investigating the scattering from more complex structures such as helicopters and other complicated platforms.

C. Electromagnetic Penetration through Composite Panels

1. Simulating EMI problems of the helicopter scale model with the FD-TD method

To simulate electromagnetic interaction and penetration problems, some of the perfectly conducting panels of the helicopter are replaced by composite material panels. Specifically, at the front section of the helicopter, tefflon with $\epsilon_r = 2.10 - j0.014$ is used. At the bottom of the helicopter, four panels are replaced by fiberglass with $\epsilon_r = 4.60 - j0.017$ at 500 MHz. The configuration of the helicopter used in this simulation is shown in Figure 8, where the composite material is shown as the shaded region. The composite materials used in this case are representative of materials used to construct modern helicopter airframes. At the frequency of 500 MHz, the composite material panels are assumed to have very small thickness compared to the wavelength of operation (typically $\lambda/500$) and so they are modeled as thin plates.

A plane wave traveling parallel to the length of the helicopter (positive x-axis), with vertical polarization (E_z and H_y components) is incident on the hybrid (perfectly conducting and composite) helicopter airframe. The amplitude of the incident electric field is assumed unity. The plane wave incident on the helicopter structure is scattered by the helicopter in all different directions. Because of the presence of some composite material panels, a significant amount of energy penetrates through the composite panels. To study the amount of penetration through the airframe, a horizontal cut was taken at a $z = \text{constant}$ plane of the helicopter model shown in Figure 8. The cross section of the horizontal cut taken is shown in Figure 9. The helicopter wings are shown as grid meshes. The incident plane wave striking the helicopter airframe is also shown in the figure. Over the horizontal cut shown in Figure 9, the amplitude distribution of the penetrating fields can be obtained. The FDTD solver allows the option to specify horizontal and vertical cuts in the problem space and obtain the amplitude and phase distribution of preselected field components. In this case, the magnetic field amplitude distributions for H_x and H_y are obtained from the FDTD solver.

In the previous progress report the same problem was solved, however, with the direction of incidence of the plane wave being in the negative x-axis. In this progress report the incidence angle is changed so that the plane wave hits the structure from the opposite direction. As will be demonstrated shortly, the penetration fields are smaller than in the previous case.

The horizontal cut taken is further divided into three separate regions (A), (B), (C) and the fields in each region are plotted separately. The results of the y- and x-components of the magnetic field distribution inside the helicopter are illustrated in Figures 10 and 11, respectively. These are normalized with respect to the amplitude of the incident magnetic field and are plotted in dB ($20 * \log_{10}(H^{total}/H^{inc})$) over the helicopter cross section. Because the incident magnetic field component is polarized in the y direction, the H_y field (co-polarization) distribution is much higher than the corresponding H_x field (cross-polarization) distribution. The fields penetrating through the helicopter in this case are smaller than the case considered in the previous progress report, where the plane wave struck head-on the composite material section of the helicopter structure.

2. Conclusions and future work

Some of the perfectly conducting panels on the helicopter structure are replaced by composite materials and the interaction of the composite airframe with a plane wave has been examined. The replacement of the perfectly conducting panels with composite ones allows the penetration of the plane wave inside the helicopter structure which acts like a cavity. The distribution of penetration fields has been examined by obtaining the x- and y-components of the magnetic-field distribution inside the helicopter.

Future work will include more elaborate study of electromagnetic penetration into more complex helicopter structures by considering inside wires, metal supports, electronic systems, or electronic housing departments. Ways to obtain the current distribution from the magnetic field distribution on the helicopter airframe are also under consideration.

In addition, radiation patterns on the helicopter structure for frequencies lower than 200 MHz, for example 20 MHz, will be attempted using the FDTD. In low frequency applications the grid size selection in the FDTD modeling has to be extremely small (less than $\lambda/100$). This small grid size creates problems in the FDTD modeling. One problem is that in FDTD sim-

ulations a distance of about one λ is left between the structure being modeled and the outer boundary of the FDTD problem space where absorbing boundary conditions are applied. This requirement will have an enormous increase in the memory needed to solve the radiation problems of low frequencies.

One way to reduce the one λ distance requirement is by using more accurate absorbing boundary conditions. The accuracy of these conditions depends on the order of approximation used. At present the second-order approximations were considered to be sufficiently accurate for the applications that were attempted. In the next reporting period progress on increasing the order of absorbing boundary conditions of up to seventh order for three dimensional problems will be reported. Hopefully, these high-order boundary conditions will allow the distance between the structure and the outer boundary to be reduced to 0.1λ , for example, and thus allow modeling of low frequency radiation problems.

D. Interaction of EM Waves With a Stratified Composite Plate

1. Introduction

The interaction of electromagnetic waves with fiber-reinforced matrix composites has gained more attention of the research community in both material and electrical science [1, 2]. The considerable interest has also been manifested in research areas of astronautics, electromagnetic engineering and space vehicle design [3, 4, 5]. In fact, there are many situations where the consideration of this interaction becomes inevitable, such as the radiation effect of composites on helicopter antennas, and electromagnetic shielding of equipment on an airplane by composite fuselage.

More specifically, graphite-epoxy composite plates are widely used to build helicopters and fighter airplanes due to their superior mechanical strength and light weight. Composite materials are anisotropic and less conductive than a metal. Therefore, when a helicopter is illuminated by an EM wave, it is easier for the EM wave to penetrate into the interior of the helicopter to cause EM interference problem. This interference may disturb the on-board electronic and computer systems. A more serious problem of the same nature is encountered when the helicopter is hit by lightning.

The complexity of a basic analysis is simply attributed to the anisotropic

electromagnetic property of the composites. Physically, the anisotropy is directly related to the orientation of fibers composing the composites. Thus the three principal axes of the permittivity and permeability, which characterize the electromagnetic properties of the composites, are found to be in parallel or perpendicular to the fiber orientation. The analysis in this report is based on the fundamental assumption that the permittivity and permeability tensors of a composite are representable by diagonal matrices.

The goal of this preliminary research is to study the electromagnetic properties of composite materials over a wide frequency band, and understand the basic electromagnetic properties of composite materials by analyzing the EM scattering behavior, or radar cross section, and the EM shielding capability of anisotropic composites. In the next research period, a proper surface impedance model is to be established, which will be coupled into the NEC and ESP codes by using the impedance loading concept.

2. Theoretical model

To simplify the analysis, we first consider a composite laminate constructed of M plies, each ply consisting of unidirectional fibers embedded in an organic matrix. The fiber orientation with respect to the x -axis is denoted by an angle θ , as shown in Figure 12. The composite is illuminated by a linearly polarized plane wave at normal incidence. The polarization angle is δ as shown in Figure 12.

In an anisotropic (conductivity $\vec{\sigma}$) medium, the Maxwell's equations are represented as

$$\nabla \times \mathbf{E} = -j\omega\mu\mathbf{H} \quad (3)$$

$$\nabla \times \mathbf{H} = \vec{\sigma} \cdot \mathbf{E} + j\omega\epsilon \cdot \mathbf{E} = j\omega \vec{\epsilon} \cdot \mathbf{E} \quad (4)$$

where the dyadic permittivity is defined as

$$\vec{\epsilon} = \frac{\vec{\sigma}}{j\omega} + \epsilon$$

ϵ is the dielectric permittivity, and μ is the permeability. Taking the curl of (1) yields

$$\nabla \times \nabla \times \mathbf{E} = -j\omega\mu \times \mathbf{H}$$

By using (4) and vector identity, we have

$$\nabla(\nabla \cdot \mathbf{E}) - \nabla^2 \mathbf{E} = -j\omega(j\omega \vec{\epsilon} \cdot \mathbf{E})$$

It can be shown that in the composite

$$\nabla \cdot \mathbf{E} = 0$$

Thus, the wave equation in the anisotropic medium takes the form of

$$\nabla^2 \mathbf{E} + \omega^2 \mu \vec{\epsilon} \cdot \mathbf{E} = 0 \quad (5)$$

In the principal coordinate system of the dyadic permittivity, the permittivity can be written as a diagonal matrix

$$\vec{\epsilon} = \begin{bmatrix} \epsilon_p^* & 0 & 0 \\ 0 & \epsilon_q^* & 0 \\ 0 & 0 & \epsilon_z^* \end{bmatrix}$$

where z -direction is defined as the propagation direction of the incident wave, p and q are the other two principal directions, and

$$\epsilon_p^* = \frac{\sigma_p}{j\omega} + \epsilon$$

$$\epsilon_q^* = \frac{\sigma_q}{j\omega} + \epsilon$$

$$\epsilon_z^* = \frac{\sigma_z}{j\omega} + \epsilon$$

In the (p, q) coordinate system, (3) can be decomposed into two components:

$$\nabla^2 E_p + \omega^2 \mu \epsilon_p E_p = 0 \quad (6)$$

$$\nabla^2 E_q + \omega^2 \mu \epsilon_q E_q = 0 \quad (7)$$

Since the incident wave is a plane wave propagating in a normal direction to the composite, the above equations simplify to

$$\frac{d^2}{dz^2} E_p + \omega^2 \mu \epsilon_p E_p = 0 \quad (8)$$

$$\frac{d^2}{dz^2} E_q + \omega^2 \mu \epsilon_q E_q = 0 \quad (9)$$

The homogeneous solution to (8) and (9) is provided by

$$E_p = E_p^+ e^{-jk_p z} + E_p^- e^{jk_p z} \quad (10)$$

$$E_q = E_q^+ e^{-jk_q z} + E_q^- e^{jk_q z} \quad (11)$$

where the superscript + denotes the forward propagating wave and the - denotes the reflected wave, and k_p and k_q are wavenumbers in p -axis and q -axis directions, which are related to electric parameters of the medium in which the wave is propagating by

$$k_p^2 = \omega^2 \mu \epsilon_p \quad (12)$$

$$k_q^2 = \omega^2 \mu \epsilon_q \quad (13)$$

Once the solution of the electric fields is obtained, the magnetic fields are deduced from

$$H = \frac{j}{\omega \mu} \nabla \times \mathbf{E}$$

Thus, we obtain

$$H_p = \frac{k_q}{\omega \mu} (E_q^+ e^{-jk_q z} - E_q^- e^{jk_q z}) \quad (14)$$

$$H_q = \frac{k_p}{\omega \mu} (E_p^+ e^{-jk_p z} - E_p^- e^{jk_p z}) \quad (15)$$

If we define

$$H_p = H_p^+ e^{-jk_q z} + H_p^- e^{jk_q z} \quad (16)$$

$$H_q = H_q^+ e^{-jk_p z} + H_q^- e^{jk_p z} \quad (17)$$

then, the amplitudes of the magnetic fields of the reflected and transmitted waves can be related to those of the electric fields by a matrix of

$$\begin{bmatrix} H_p^+ \\ H_q^+ \end{bmatrix} = \frac{1}{\sqrt{\mu}} \begin{bmatrix} -\sqrt{\epsilon_q^*} & 0 \\ 0 & \sqrt{\epsilon_p^*} \end{bmatrix} \begin{bmatrix} E_q^+ \\ E_p^+ \end{bmatrix} \quad (18)$$

and

$$\begin{bmatrix} H_p^- \\ H_q^- \end{bmatrix} = -\frac{1}{\sqrt{\mu}} \begin{bmatrix} -\sqrt{\epsilon_q^*} & 0 \\ 0 & \sqrt{\epsilon_p^*} \end{bmatrix} \begin{bmatrix} E_q^- \\ E_p^- \end{bmatrix} \quad (19)$$

Consider a plane wave incident on the interface between two media as shown in Figure 12. The components of the electric fields in the medium a with respect to the global coordinate system (x_1, x_2) can be projected on to the principal coordinate system of the medium a by

$$\begin{bmatrix} E_1^i \\ E_2^i \end{bmatrix} = \begin{bmatrix} \cos\theta_a & -\sin\theta_a \\ \sin\theta_a & \cos\theta_a \end{bmatrix} \begin{bmatrix} E_p^i \\ E_q^i \end{bmatrix} \quad (20)$$

and the magnetic fields are projected as

$$\begin{bmatrix} H_1^i \\ H_2^i \end{bmatrix} = \begin{bmatrix} \cos\theta_a & -\sin\theta_a \\ \sin\theta_a & \cos\theta_a \end{bmatrix} \begin{bmatrix} H_p^i \\ H_q^i \end{bmatrix} \quad (21)$$

by using (18), (21) reduces to

$$\begin{bmatrix} H_1^i \\ H_2^i \end{bmatrix} = \begin{bmatrix} \cos\theta_a & -\sin\theta_a \\ \sin\theta_a & \cos\theta_a \end{bmatrix} \frac{1}{\sqrt{\mu}} \begin{bmatrix} \sqrt{\epsilon_q^*} & 0 \\ 0 & \sqrt{\epsilon_p^*} \end{bmatrix} \begin{bmatrix} E_q^+ \\ E_p^+ \end{bmatrix} \quad (22)$$

$$\begin{bmatrix} H_1^i \\ H_2^i \end{bmatrix} = \frac{1}{\sqrt{\mu}} \begin{bmatrix} \cos\theta_a & -\sin\theta_a \\ \sin\theta_a & \cos\theta_a \end{bmatrix} \begin{bmatrix} 0 & \sqrt{\epsilon_q^*} \\ \sqrt{\epsilon_p^*} & 0 \end{bmatrix} \begin{bmatrix} E_q^i \\ E_p^i \end{bmatrix} \quad (23)$$

$$\begin{bmatrix} H_1^i \\ H_2^i \end{bmatrix} = \frac{1}{\sqrt{\mu}} \begin{bmatrix} \cos\theta_a & -\sin\theta_a \\ \sin\theta_a & \cos\theta_a \end{bmatrix} \begin{bmatrix} 0 & \sqrt{\epsilon_q^*} \\ \sqrt{\epsilon_p^*} & 0 \end{bmatrix} \begin{bmatrix} \cos\theta_a & \sin\theta_a \\ -\sin\theta_a & \cos\theta_a \end{bmatrix} \begin{bmatrix} E_1^i \\ E_2^i \end{bmatrix} \quad (24)$$

$$\begin{bmatrix} H_1^i \\ H_2^i \end{bmatrix} = N_a \begin{bmatrix} E_1^i \\ E_2^i \end{bmatrix} \quad (25)$$

where N_a is called the characteristic matrix for the medium a . Following the same procedure, similar relations for the reflected and transmitted waves can be established, that is,

$$\begin{bmatrix} H_1^r \\ H_2^r \end{bmatrix} = -N_a \begin{bmatrix} E_1^r \\ E_2^r \end{bmatrix} \quad (26)$$

$$\begin{bmatrix} H_1^t \\ H_2^t \end{bmatrix} = N_b \begin{bmatrix} E_1^t \\ E_2^t \end{bmatrix} \quad (27)$$

with N_b is the characteristic matrix of the medium b .

Without the loss of generality, the interface of the media a and b is assumed to be located at the plane of $z = 0$. Matching the tangential components of the electric and magnetic fields on the interface leads to

$$\begin{bmatrix} E_1^i \\ E_2^i \end{bmatrix} - \begin{bmatrix} E_1^t \\ E_2^t \end{bmatrix} = - \begin{bmatrix} E_1^r \\ E_2^r \end{bmatrix} \quad (28)$$

and

$$\begin{bmatrix} H_1^i \\ H_2^i \end{bmatrix} - \begin{bmatrix} H_1^t \\ H_2^t \end{bmatrix} = - \begin{bmatrix} H_1^r \\ H_2^r \end{bmatrix} \quad (29)$$

Using the above results, we can write it out

$$N_a \begin{bmatrix} E_1^i \\ E_2^i \end{bmatrix} - N_b \begin{bmatrix} E_1^t \\ E_2^t \end{bmatrix} = N_a \begin{bmatrix} E_1^r \\ E_2^r \end{bmatrix} \quad (30)$$

Solving simultaneously (28) and (30) leads to

$$\begin{bmatrix} E_1^r \\ E_2^r \end{bmatrix} = [N_a + N_b]^{-1} [N_a - N_b] \begin{bmatrix} E_1^i \\ E_2^i \end{bmatrix} \quad (31)$$

and

$$\begin{bmatrix} E_1^t \\ E_2^t \end{bmatrix} = 2[N_a + N_b]^{-1} N_a \begin{bmatrix} E_1^i \\ E_2^i \end{bmatrix} \quad (32)$$

In the preceding discussions, the wave is incident from one side only. As shown in Figure 13, if waves are incident from both sides of the interface, their reflected and transmitted counterparts are given by

$$\mathbf{E}_i^+ = \mathbf{E}_t^+ - \mathbf{E}_r^+ \quad (33)$$

$$\mathbf{E}_i^- = \mathbf{E}_t^- - \mathbf{E}_r^- \quad (34)$$

It is helpful to define the effective reflected and transmitted waves here as

$$\mathbf{P}^+ = \mathbf{E}_t^+ + \mathbf{E}_r^- \quad (35)$$

$$\mathbf{P}^- = \mathbf{E}_t^- + \mathbf{E}_r^+ \quad (36)$$

Since the reflected waves can be characterized by reflection coefficients as

$$\mathbf{E}_r^+ = \vec{r} \cdot \mathbf{E}_i^+ \quad (37)$$

$$\mathbf{E}_r^- = -\vec{r} \cdot \mathbf{E}_i^- \quad (38)$$

where \vec{r} is the reflection dyadic from the medium a to the medium b , which can be represented by the characteristic matrix as

$$\vec{r} = [N_a + N_b]^{-1} [N_a - N_b]$$

Consequently, the effective reflected and transmitted electric fields can be represented in terms of the reflection dyadic by

$$\begin{aligned} \mathbf{P}^+ &= \mathbf{E}_t^+ + (-\vec{r} \cdot \mathbf{E}_i^-) = \mathbf{E}_i^+ + \mathbf{E}_r^+ - \vec{r} \cdot \mathbf{E}_i^- \\ &= (\vec{I} + \vec{r}) \cdot \mathbf{E}_i^+ - \vec{r} \cdot \mathbf{E}_i^- \end{aligned} \quad (39)$$

$$\begin{aligned} \mathbf{P}^- &= \mathbf{E}_t^- + \vec{r} \cdot \mathbf{E}_i^+ \\ &= -\mathbf{E}_i^- - \mathbf{E}_r^- + \vec{r} \cdot \mathbf{E}_i^+ \end{aligned} \quad (40)$$

$$= (\vec{I} - \vec{r}) \cdot \mathbf{E}_i^- + \vec{r} \cdot \mathbf{E}_i^+ \quad (41)$$

Up to this point, we have considered only the case of reflection by and transmission through one interface between two media. If the composite is a multi-layered structure, the solution of the electric fields in different media can be obtained in a similar way. Considering two adjacent interfaces as shown in Figure 14, we use the subscript $m-1$ to denote the interface between the $(m-1)$ th ply and m th ply. Inside the m th ply of the composite, the electric fields at the $(m-1)$ th interface are related to that at the m th interface by a transmission matrix A_m as

$$(\mathbf{E}_i^+)_m = A_m \mathbf{P}_m^+ \quad (42)$$

$$(\mathbf{E}_i^-)_m = A_m \mathbf{P}_m^- \quad (43)$$

where

$$A_m = \begin{bmatrix} \cos\theta_a & -\sin\theta_a \\ \sin\theta_a & \cos\theta_a \end{bmatrix} \begin{bmatrix} e^{jk_p d_m} & 0 \\ 0 & e^{-jk_q d_m} \end{bmatrix} \begin{bmatrix} \cos\theta_a & \sin\theta_a \\ -\sin\theta_a & \cos\theta_a \end{bmatrix} \quad (44)$$

If there are M layers in the composite, based on the previous formulations, the effective reflected and transmitted electric fields inside the m th ply can be represented by that inside the two adjacent plies as

$$\mathbf{P}_m^+ = (\vec{I} + \vec{r}_m) A_{m-1} \mathbf{P}_{m-1}^+ - \vec{r}_m A_m \mathbf{P}_{m+1}^- \quad (45)$$

and

$$\mathbf{P}_m^- = (\vec{I} - \vec{r}_m) A_m \mathbf{P}_{m+1}^+ + \vec{r}_m A_{m-1} \mathbf{P}_{m-1}^- \quad (46)$$

Since the excitation wave is incident on to the first interface, applying 45 and 46 at the first interface yields

$$\mathbf{P}_1^+ = (\vec{I} + \vec{r}_1) \mathbf{E}_{inc} - \vec{r}_1 A_1 \mathbf{P}_2^- \quad (47)$$

$$\mathbf{P}_1^- = (\vec{I} - \vec{r}_1) A_1 \mathbf{P}_2^- + \vec{r}_1 \mathbf{E}_{inc} \quad (48)$$

or

$$\mathbf{P}_1^+ - \mathbf{P}_1^- + A_1 \mathbf{P}_2^- = \mathbf{E}_{inc} \quad (49)$$

$$\mathbf{P}_1^+ + \vec{r}_1 A_1 \mathbf{P}_2^- = (\vec{I} + \vec{r}_1) \cdot \mathbf{E}_{inc} \quad (50)$$

where \mathbf{E}_{inc} denotes the excitation electric field. Similarly, at the interface of $m = M + 1$, we obtain

$$\mathbf{P}_{M+1}^+ = (\vec{I} + \vec{r}_{M+1}) A_M \mathbf{P}_M^+ \quad (51)$$

$$\mathbf{P}_{M+1}^- = \vec{r}_{M+1} A_M \mathbf{P}_M^+ \quad (52)$$

or

$$A_M \mathbf{P}_M^+ - \mathbf{P}_{M+1}^+ + \mathbf{P}_{M+1}^- = 0 \quad (53)$$

$$\vec{r}_{M+1} A_M \mathbf{P}_M^+ - \mathbf{P}_{M+1}^- = 0 \quad (54)$$

In general, at the m th interface, we have

$$(\vec{I} + \vec{r}_m) A_{m-1} \mathbf{P}_{m-1}^+ - \mathbf{P}_m^+ - \vec{r}_m A_m \mathbf{P}_{m+1}^- = 0 \quad (55)$$

$$\vec{r}_m A_{m-1} \mathbf{P}_{m-1}^+ - \mathbf{P}_m^- + (\vec{I} + \vec{r}_m) A_m \mathbf{P}_{m+1}^- = 0 \quad (56)$$

In fact, the effective reflected and transmitted electric fields also can be represented by a cascaded matrix form that relates the fields at one interface

to that at another interface. Thus, the solution of the total reflected and transmitted fields can be achieved by inverting the cascaded matrix.

Consider the $(M + 1)$ th interface, from equations (51) and (52), we have

$$\mathbf{P}_M^+ = [(\vec{I} + \vec{r}_{M+1})A_M]^{-1}\mathbf{P}_{M+1}^+ \quad (57)$$

and

$$\mathbf{P}_{M+1}^- = \vec{r}_{M+1} A_M [(\vec{I} + \vec{r}_{M+1})A_M]^{-1}\mathbf{P}_{M+1}^+ \quad (58)$$

which can be written in a matrix form as

$$\begin{aligned} \begin{bmatrix} \mathbf{P}_M^+ \\ \mathbf{P}_{M+1}^- \end{bmatrix} &= \begin{bmatrix} [(\vec{I} + \vec{r}_{M+1})A_M]^{-1} & 0 \\ \vec{r}_{M+1} A_M [(\vec{I} + \vec{r}_{M+1})A_M]^{-1} & 0 \end{bmatrix} \begin{bmatrix} \mathbf{P}_{M+1}^+ \\ 0 \end{bmatrix} \\ &= Z_{M+1} \begin{bmatrix} \mathbf{P}_{M+1}^+ \\ 0 \end{bmatrix} \end{aligned} \quad (59)$$

Equation (59) is a special form at the $(M + 1)$ th interface. In general, the effective reflected and transmitted electric fields at one interface are represented by that at the next interface as

$$\begin{bmatrix} \mathbf{P}_{m-1}^+ \\ \mathbf{P}_m^- \end{bmatrix} = Z_M \begin{bmatrix} \mathbf{P}_{M+1}^+ \\ \mathbf{P}_{M-1}^- \end{bmatrix} \quad (60)$$

where

$$Z_M = \begin{bmatrix} a & b \\ c & d \end{bmatrix}$$

with

$$\begin{aligned} a &= [(\vec{I} + \vec{r}_m)A_{m-1}]^{-1} \\ b &= [(\vec{I} + \vec{r}_m)A_{m-1}]^{-1} \vec{r}_m A_m \\ c &= \vec{r}_m A_{m-1} [(\vec{I} + \vec{r}_m)A_{m-1}]^{-1} \\ d &= (\vec{I} - \vec{r}_m)^{-1} A_m + \vec{r}_m A_{m-1} [(\vec{I} + \vec{r}_m)A_{m-1}]^{-1} \vec{r}_m A_m \end{aligned}$$

Based on these equations, we can relate the total reflected and transmitted electric fields to the external excitation as

$$\begin{bmatrix} \mathbf{E}_{inc} \\ \mathbf{P}_1^- \end{bmatrix} = \begin{bmatrix} (\vec{I} + \vec{r}_1)^{-1} & (\vec{I} + \vec{r}_1)^{-1} \vec{r}_1 A_1 \\ \vec{r}_1 (\vec{I} + \vec{r}_1)^{-1} & (\vec{I} - \vec{r}_1)^{-1} A_1 + \vec{r}_1 (\vec{I} + \vec{r}_1)^{-1} \vec{r}_1 A_1 \end{bmatrix} \begin{bmatrix} \mathbf{P}_1^+ \\ \mathbf{P}_2^- \end{bmatrix} \quad (61)$$

$$\begin{bmatrix} \mathbf{E}_{inc} \\ \mathbf{P}_1^- \end{bmatrix} = Z_0 \cdot Z_1 \cdot Z_2 \cdots \cdots Z_{M+1} \begin{bmatrix} \mathbf{P}_{M+1}^+ \\ 0 \end{bmatrix} \quad (62)$$

$$\begin{bmatrix} \mathbf{E}_{inc} \\ \mathbf{P}_1^- \end{bmatrix} = \mathbf{Z} \cdot \begin{bmatrix} \mathbf{P}_{M+1}^+ \\ 0 \end{bmatrix} \quad (63)$$

$$\begin{bmatrix} \mathbf{E}_{inc} \\ \mathbf{P}_1^- \end{bmatrix} = \begin{bmatrix} z_{11} & z_{21} \\ z_{21} & z_{22} \end{bmatrix} \begin{bmatrix} \mathbf{P}_{M+1}^+ \\ 0 \end{bmatrix} \quad (64)$$

Thus, the total reflected and transmitted electric fields are given by

$$\mathbf{P}_1^- = z_{21} \cdot z_{11}^{-1} \cdot \mathbf{E}_{inc} \quad (65)$$

and

$$\mathbf{P}_{M+1}^+ = z_{11}^{-1} \cdot \mathbf{E}_{inc} \quad (66)$$

The total reflectance R and transmittance T are then determined by

$$R = \frac{|\mathbf{P}_1^-|^2}{|\mathbf{E}_{inc}|^2} \quad (67)$$

$$T = \frac{|\mathbf{P}_{M+1}^+|^2}{|\mathbf{E}_{inc}|^2} \quad (68)$$

Equations (59) to (68) are fundamental relations used to analyze the reflection and transmission characteristic of a stratified composite illuminated by plane electromagnetic wave at normal incidence. Extensive numerical simulations have already been conducted. Typical examples are illustrated in the following section.

3. Numerical examples

This section presents various numerical simulations of the interaction of a plane wave with a multi-layered composite structure. The electric parameters are cited from reference [1], and are assumed to be valid in the frequency band of interest.

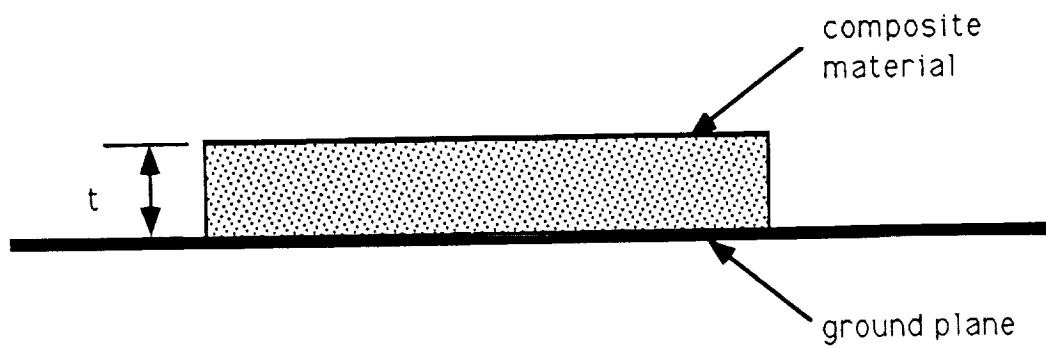
First, we try to obtain the scattering characteristics of a one-layered prepreg AS/3501-6. Different polarizations of the incident electric fields with respect to the fiber running direction are used to calculate the total reflectance and transmittance. Figure 15 shows the reflectance of a one-layered

prepreg before curing when an incident electromagnetic wave is illuminated at relative polarization angles of 0° , 45° , and 90° . As the frequency of the incident wave is increased, we observe that the reflectance at 0° approaches unity very rapidly. However, the reflectance at the other polarization angles is relatively small, even when the frequency is up to 4 GHz. Thus, we see that the reflectance is strongly dependent on the polarization of the incident field. Figure 16 shows the transmittance of the specified structure. At 0° excitation, the transmittance is very small when the frequency is above 1 GHz. At 90° excitation, the transmittance is much larger. Especially at low frequency end, it is very close to unity, which implies the transparency of the structure to the incident wave.

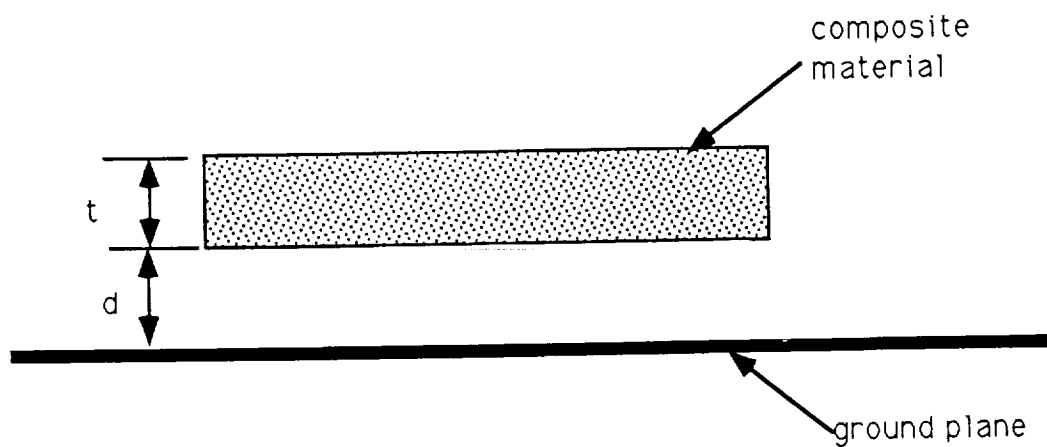
Figures 17 and 18 show the results of two-layered structure that consists of two plies of prepregs placed so that the fiber orientations of each ply are in parallel. The same polarization-dependency of the incident field is also observed. The penetration of the electric field, which is perpendicular to the fiber orientation, is also dominant especially at the low frequency range.

Figures 19 and 20 show the comparison of the reflectances and transmittances between different layers of composite prepregs. The fiber direction of one prepreg is perpendicular to that of the adjacent prepregs. The curves are shown for two-layered, eight-layered and sixteen-layered structures which are illuminated by a 45° -polarized electromagnetic wave. As we observed, when the frequency is beyond 0.6 GHz, the transmittance is very close to zero. In other words, if the frequency is higher than 0.6 GHz, the wave penetration is negligible. But, at the low frequency range, the penetration can be overwhelming even though sixteen-layered plates are used. For a helicopter to prevent the penetration of lightning, special construction is needed.

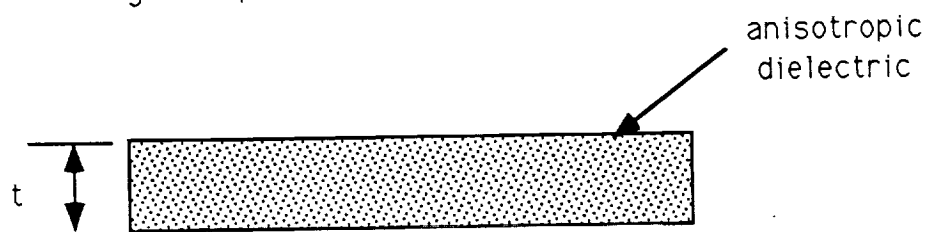
Figures 21 and 22 show the reflectance and transmittance of two-layered and 45° crossed prepregs when the incident electric field is polarized at different angles. It is seen that once there is a ply that has a fiber direction in parallel to the polarization of the incident electric field, the transmittance of the entire plate becomes very small at frequencies higher than 1 GHz. The strong dependency on the polarization of incident fields is again observed.



(a) Metal backed composite material



(b) Composite material with a distant ground plane



(c) Composite material without metal backing

Figure 1: Modeling geometry of a composite plate

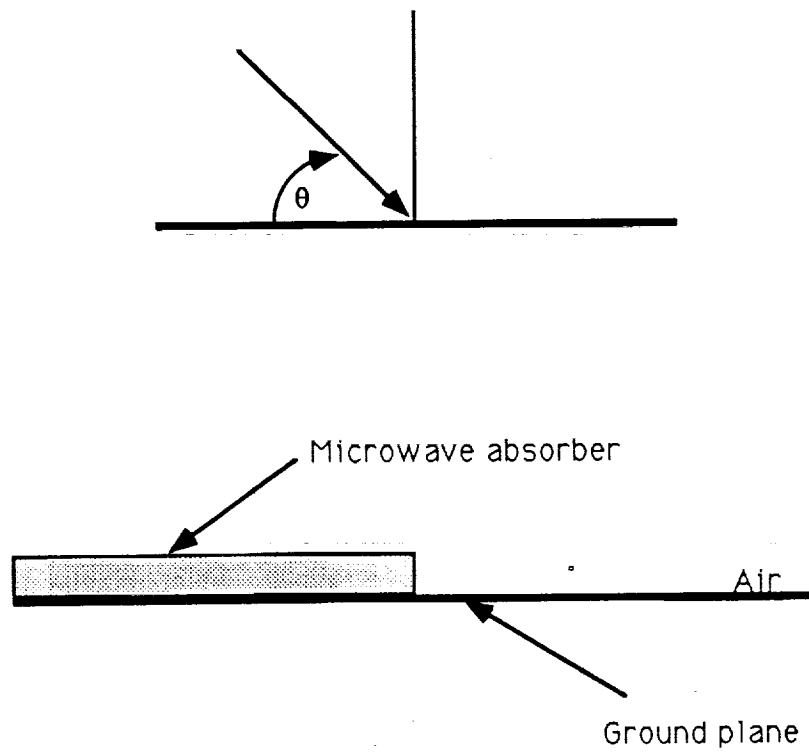


Figure 2: Modeling geometry of a PEC partially covered by GDS

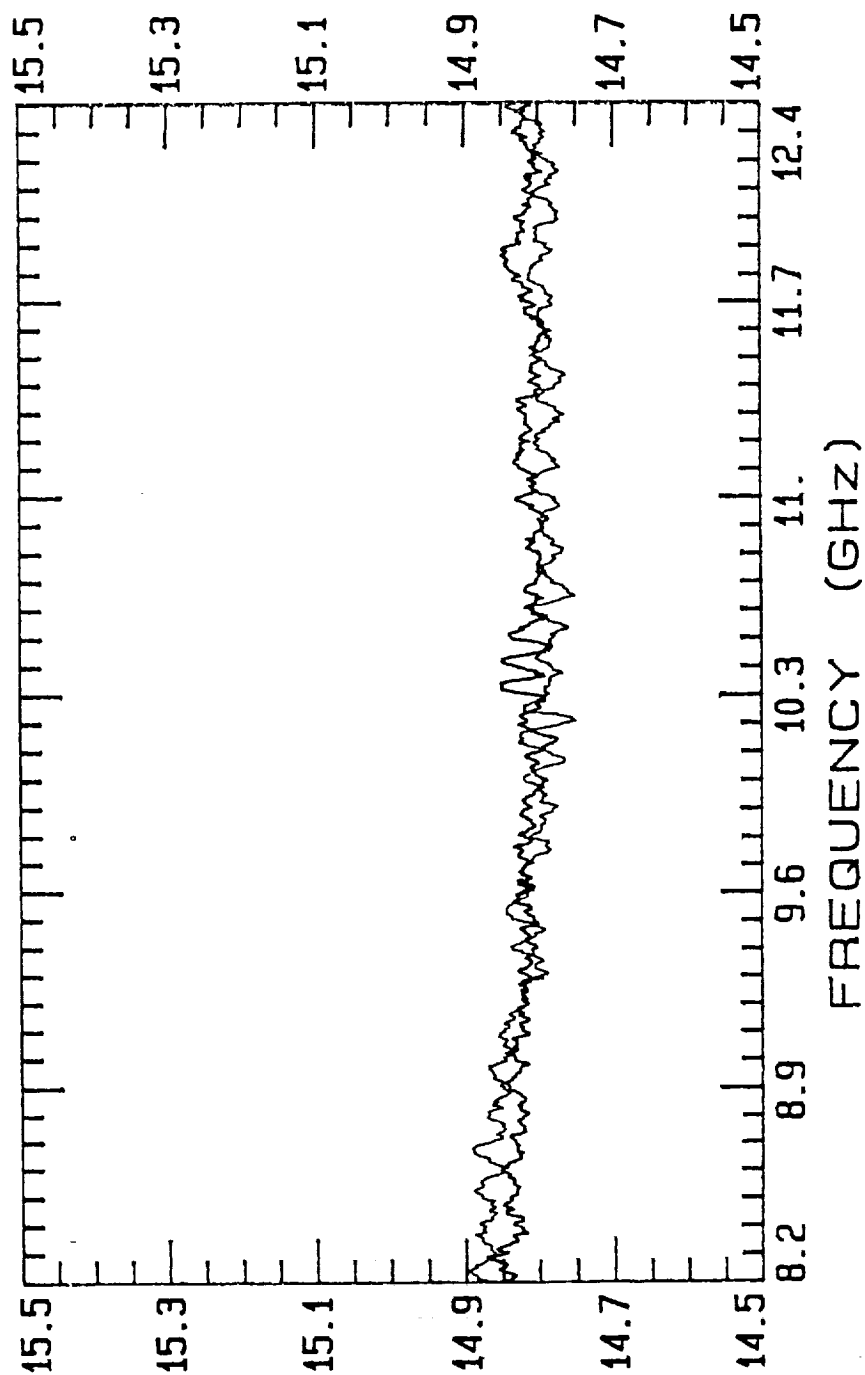


Figure 3: Measured real part of the permittivity of GDS

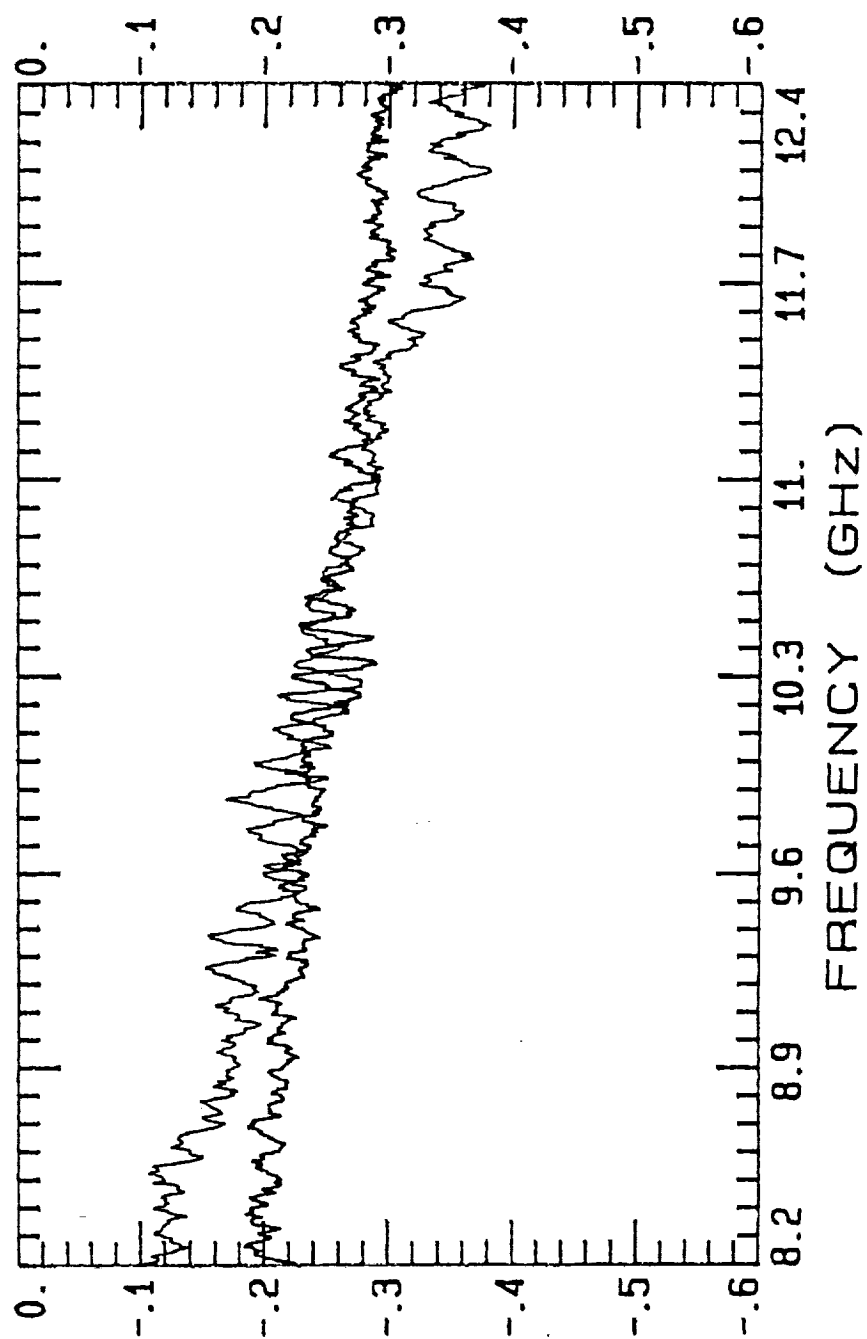


Figure 4: Measured imaginary part of the permittivity of GDS

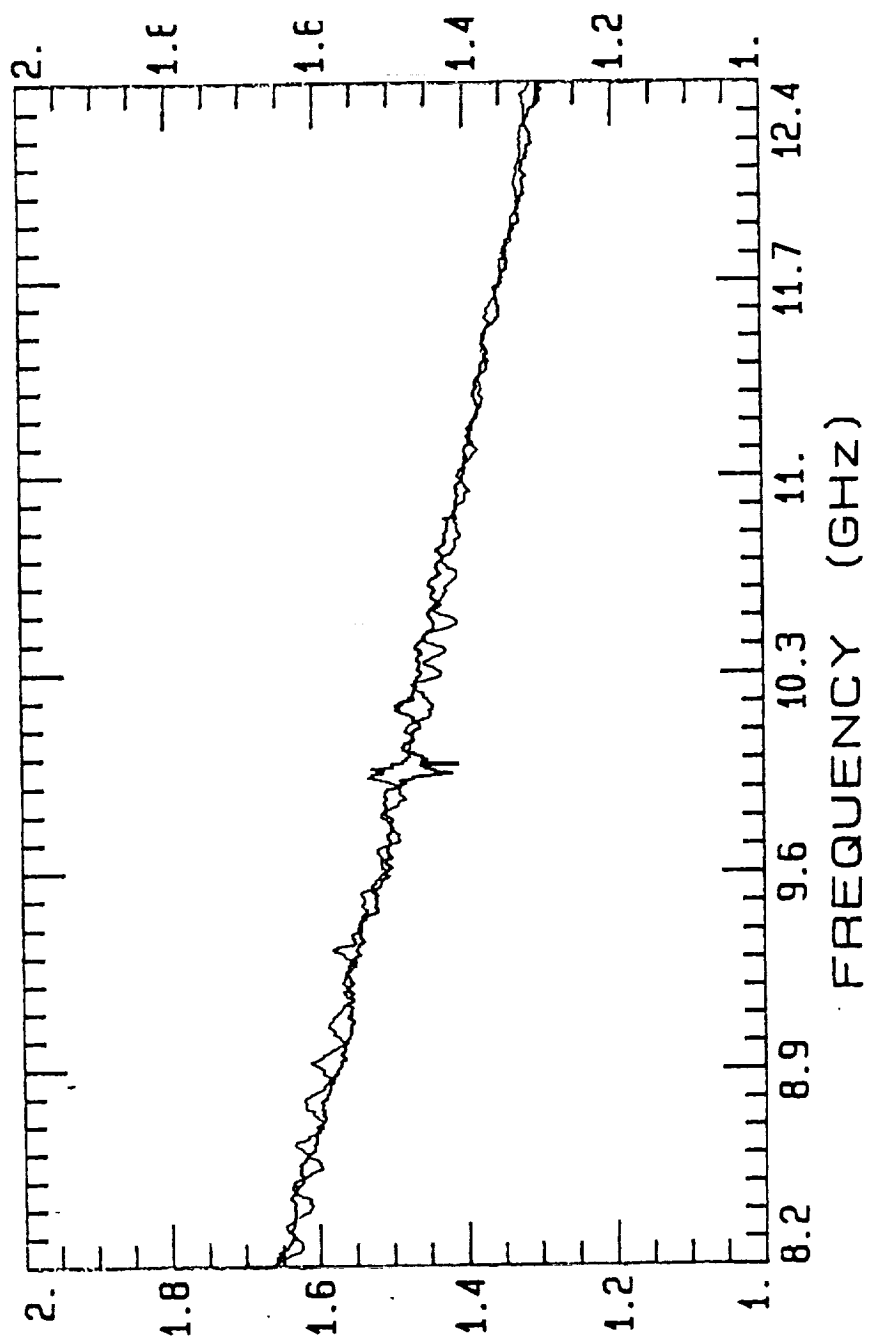


Figure 5: Measured real part of the permeability of GDS

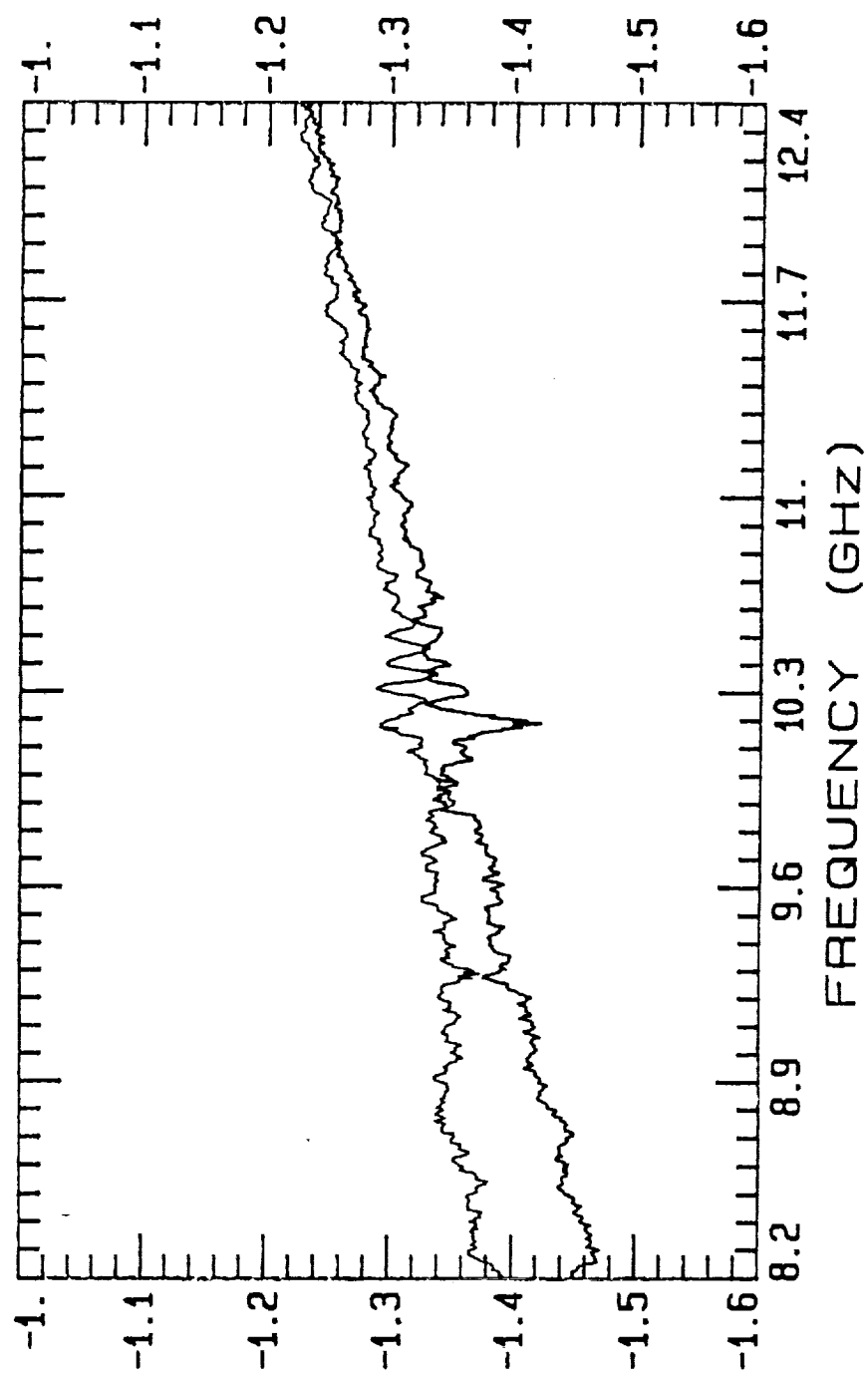


Figure 6: Measured imaginary part of the permeability of GDS

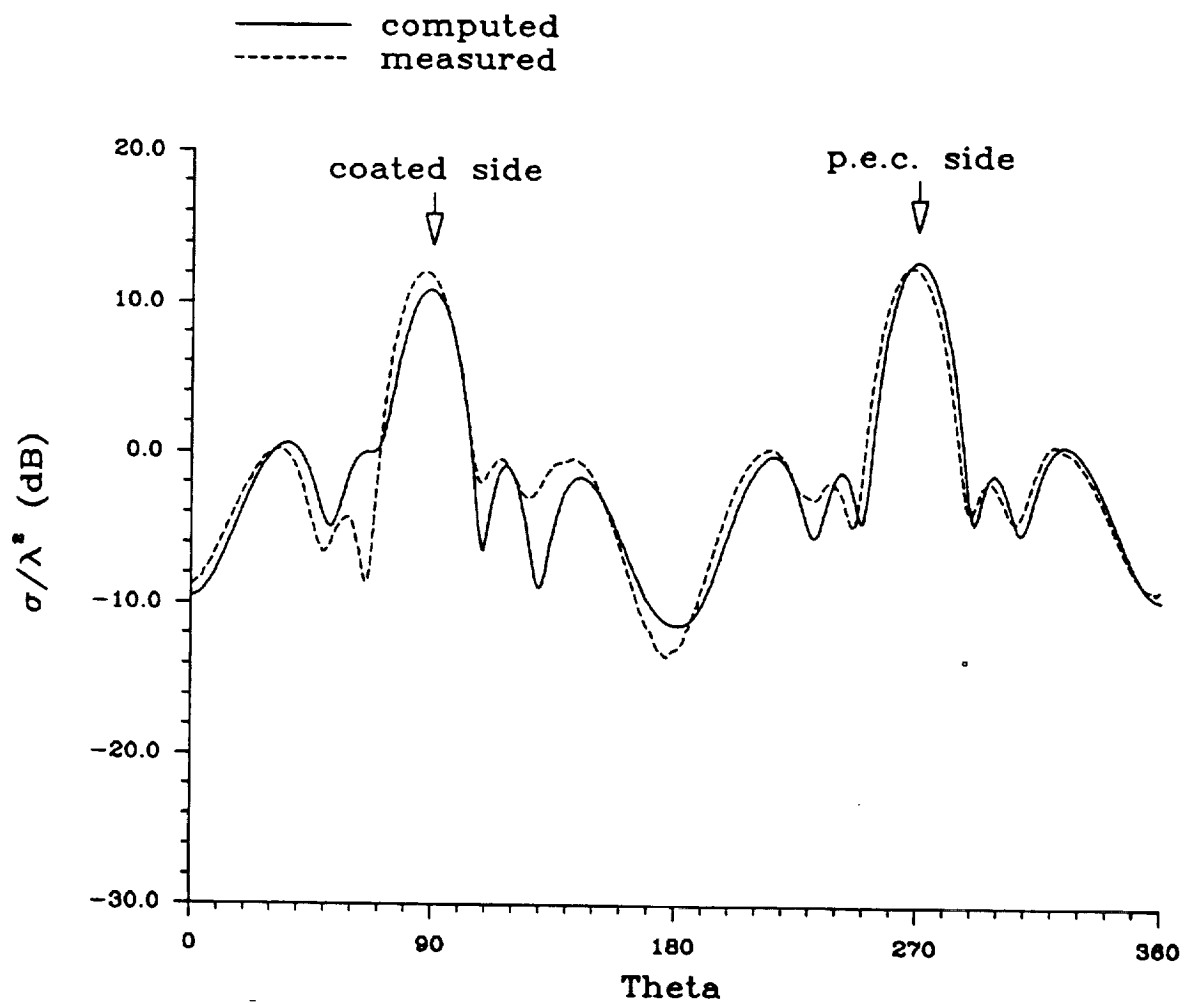


Figure 7: Comparison between computed and measured patterns of a PEC plate partially covered by GDS

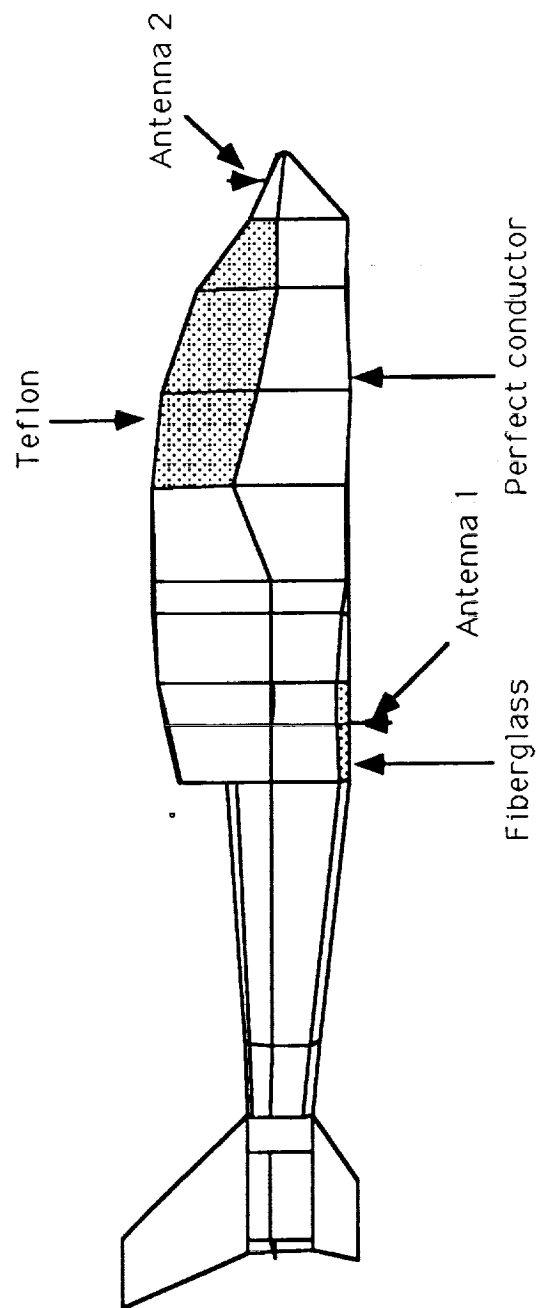


Figure 8: Partially-conducting/partially-composite material structure used to study electromagnetic penetration into the helicopter airframe.

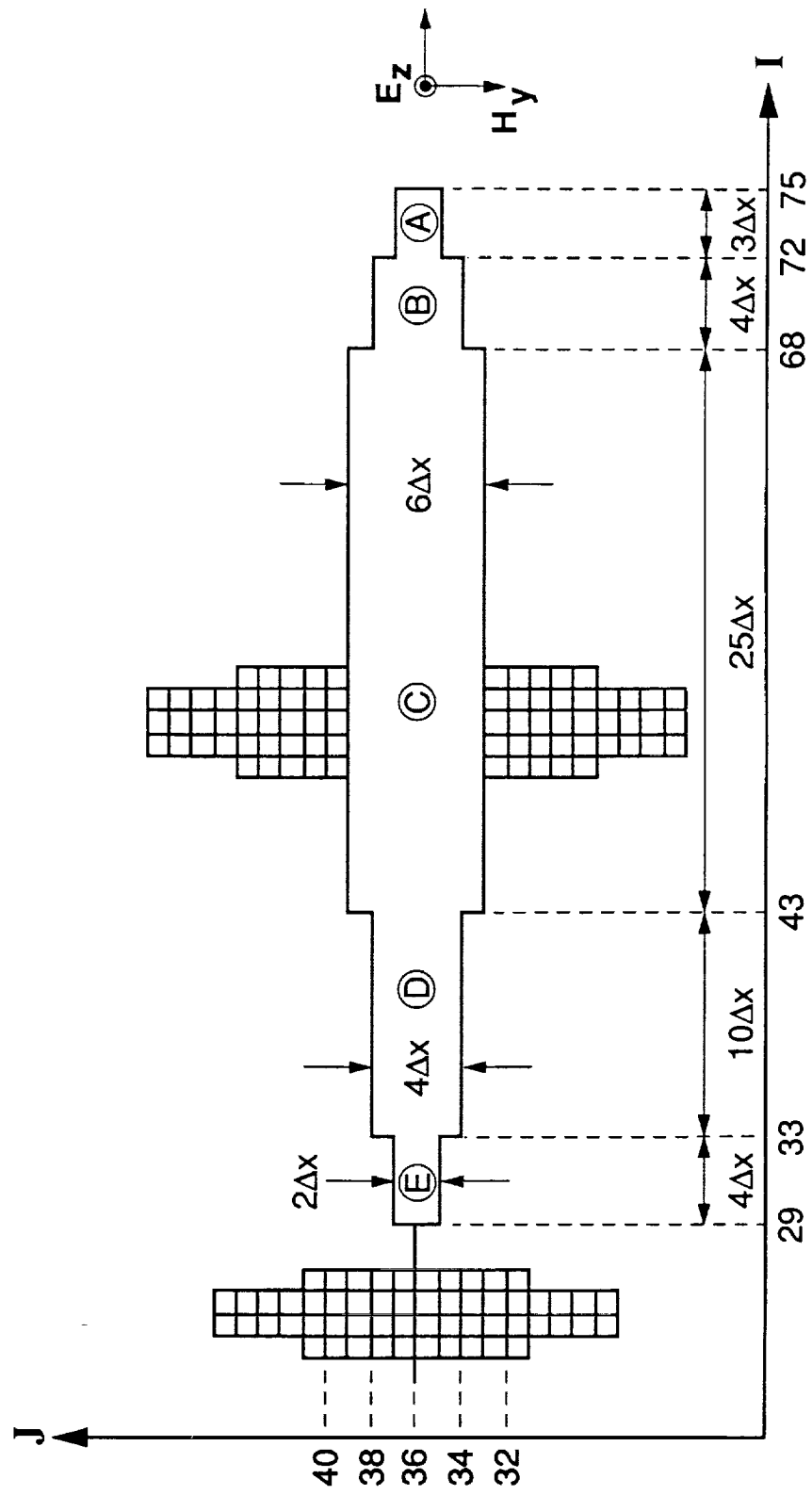


Figure 9: Helicopter cross section at a constant z plane. The magnetic field distributions in regions (A), (B), (C) are obtained from the FDTD solver.

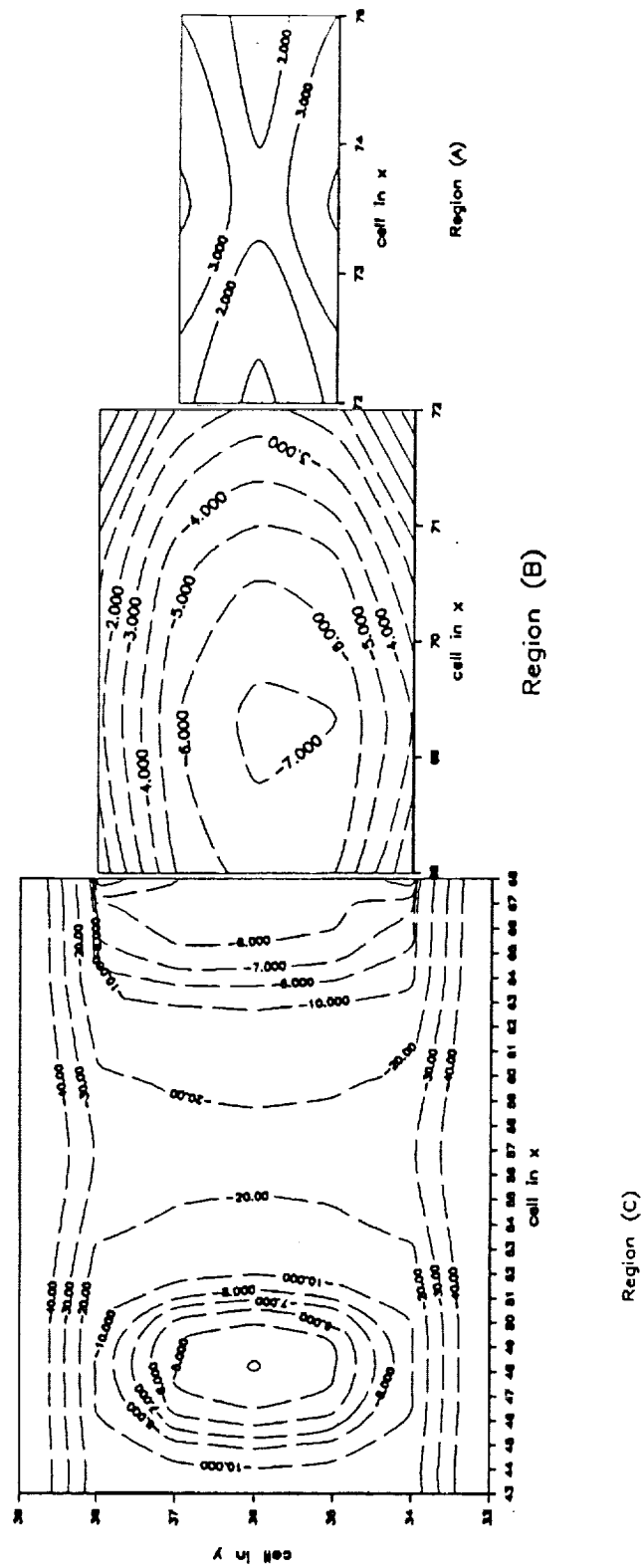


Figure 10: H_y magnetic field distribution inside the helicopter structure at 500 MHz.

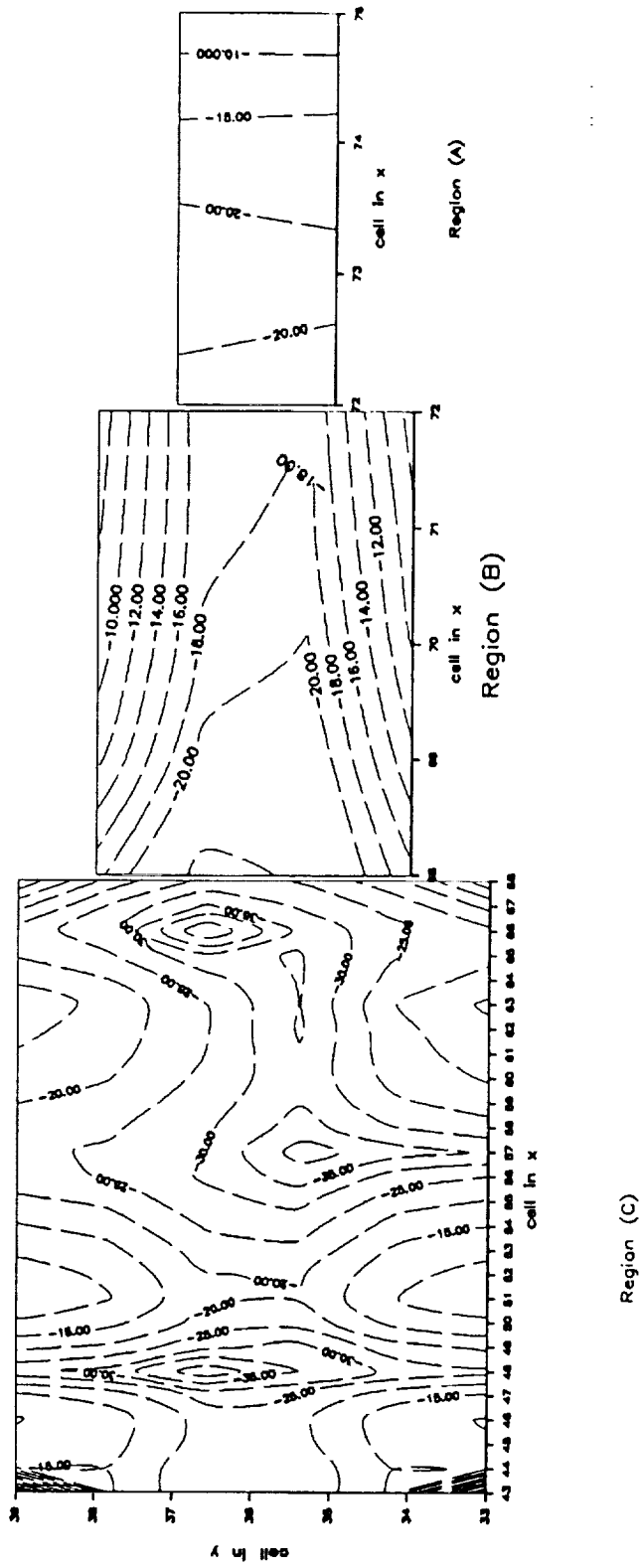


Figure 11: H_x magnetic field distribution inside the helicopter structure at 500 MHz.

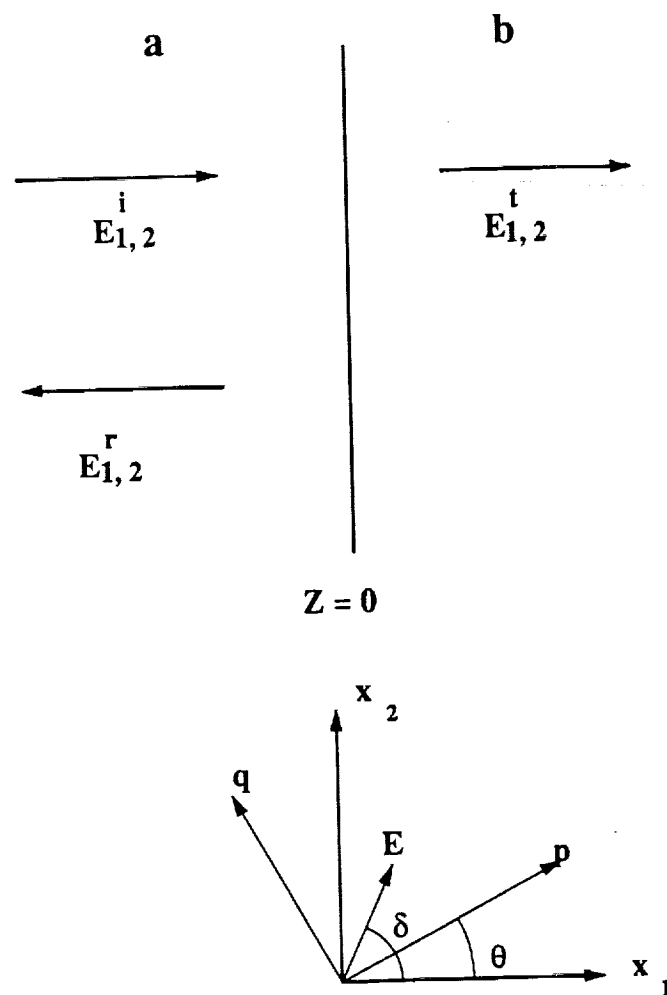


Figure 12: Incident, reflected and transmitted fields by an interface between media a and b .

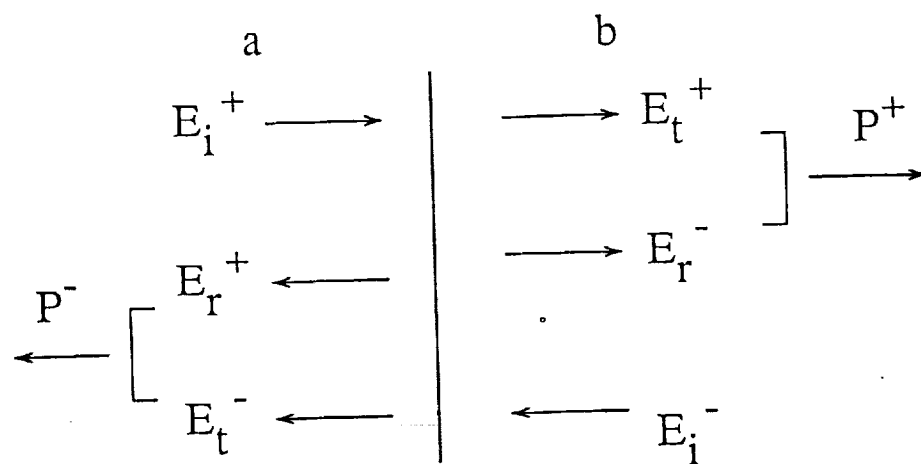


Figure 13: Effective reflected and transmitted fields on an interface between two media.

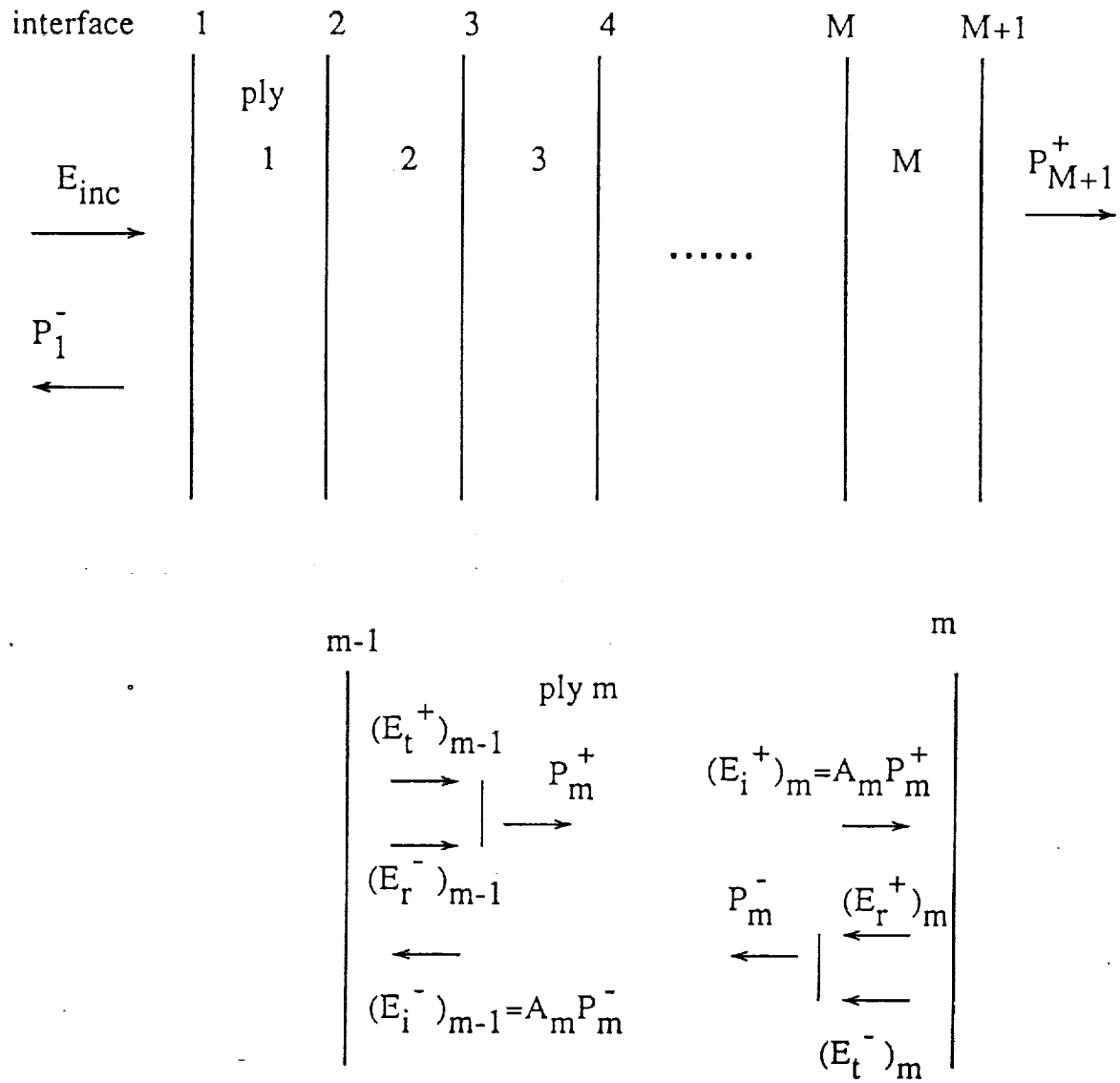


Figure 14: Reflection and transmission of the electric fields by multi composite layers

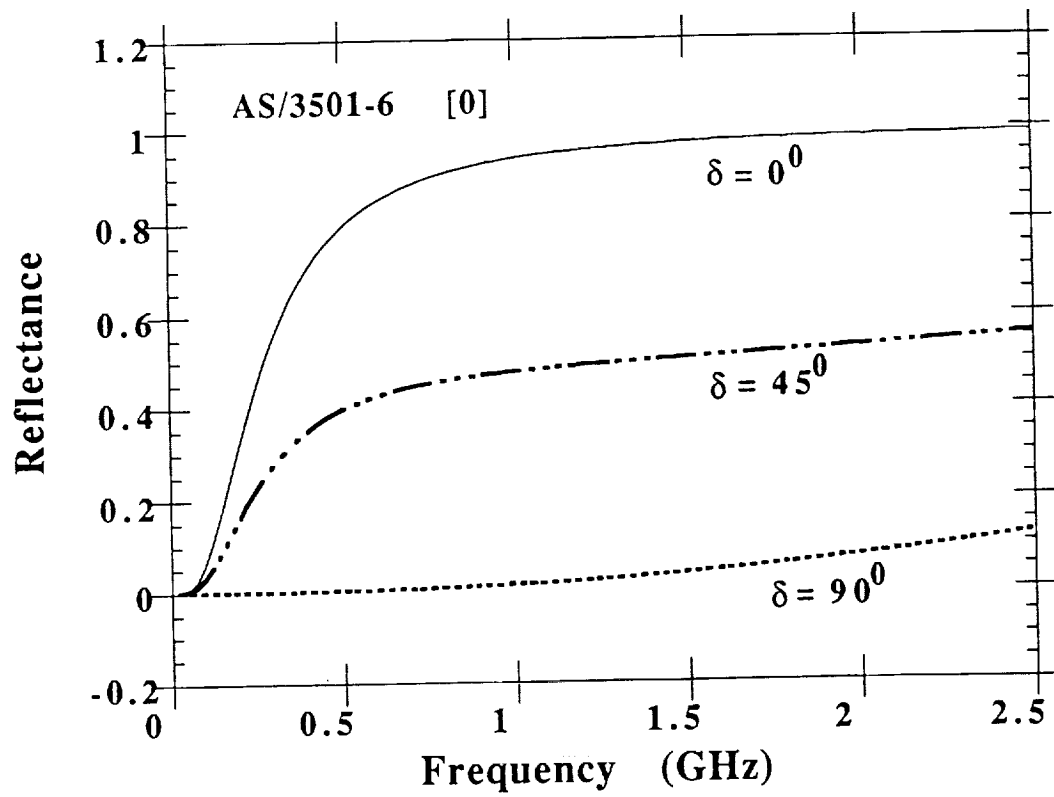


Figure 15: The reflectance of a one-ply AS/3501-6 composite plate illuminated by an incident wave polarized at 0° , 45° and 90°

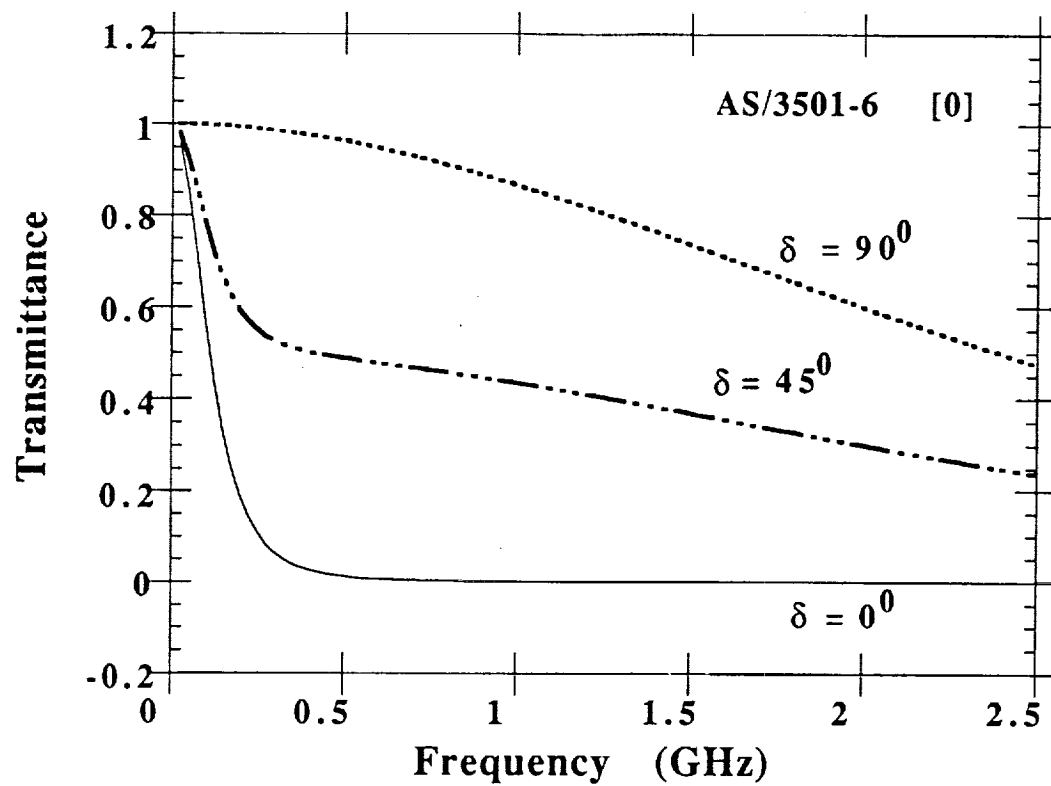


Figure 16: The transmittance of a one-ply AS/3501-6 composite plate illuminated by an incident wave polarized at 0° , 45° and 90°

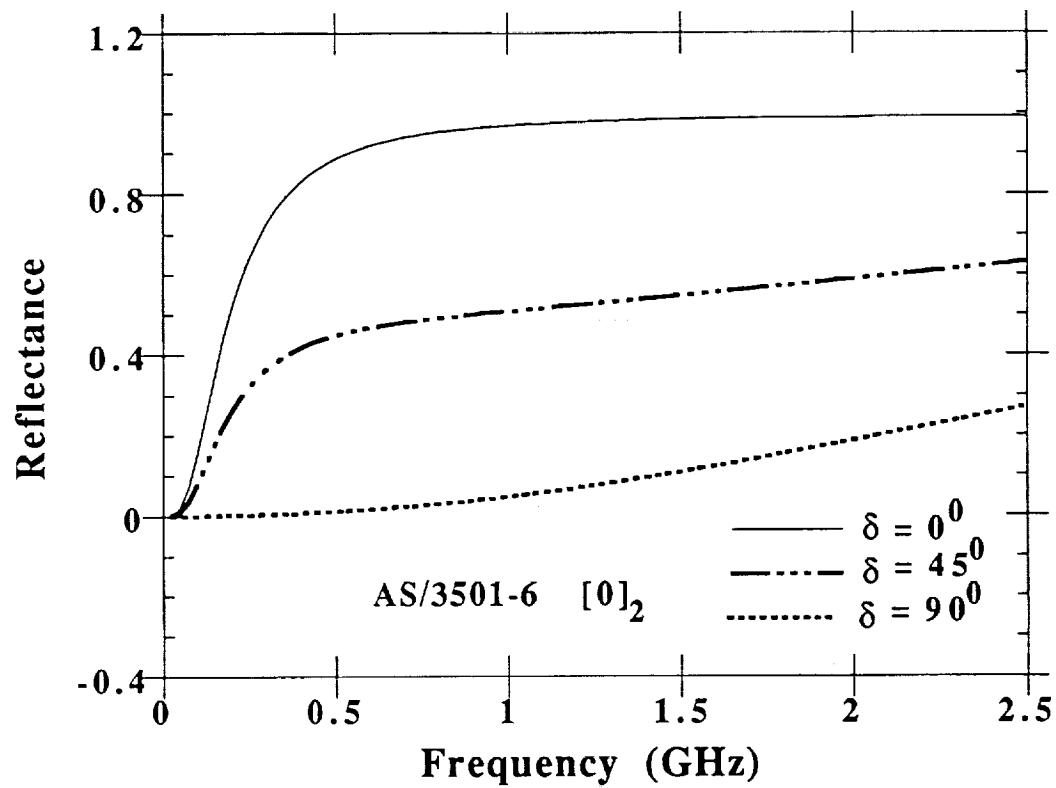


Figure 17: The reflectance of a two-ply AS/3501-6 composite plate illuminated by an incident wave polarized at 0° , 45° and 90°

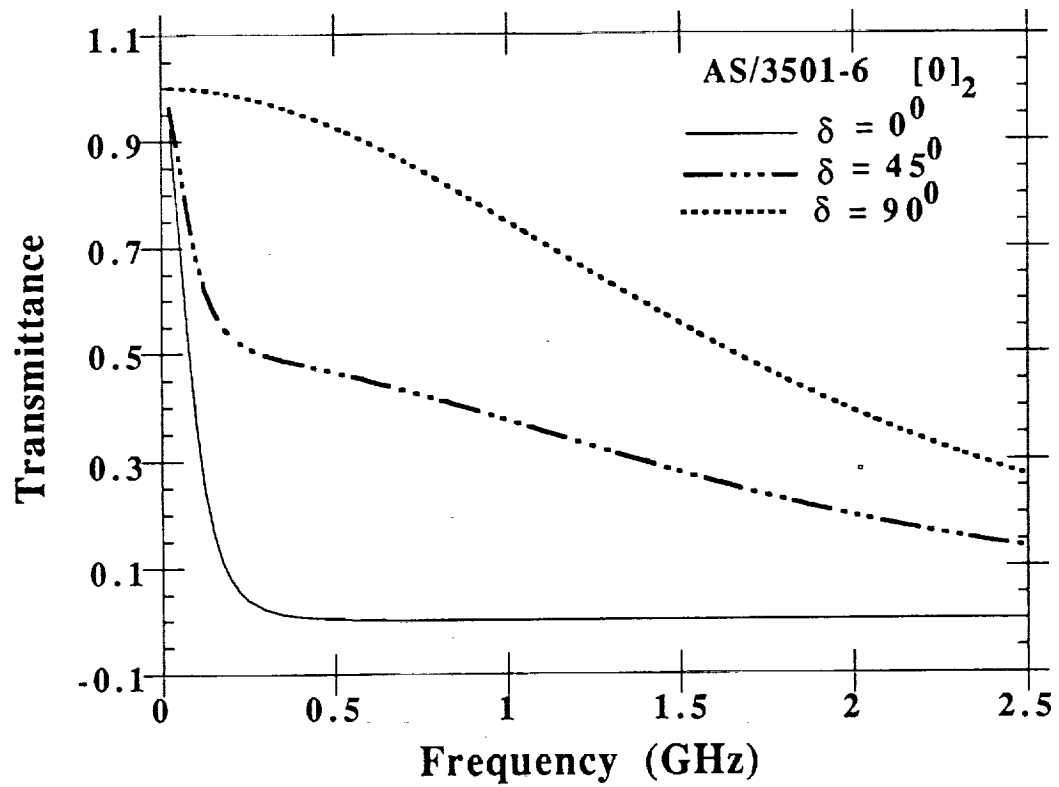


Figure 18: The transmittance of a two-ply AS/3501-6 composite plate illuminated by an incident wave polarized at 0° , 45° and 90°

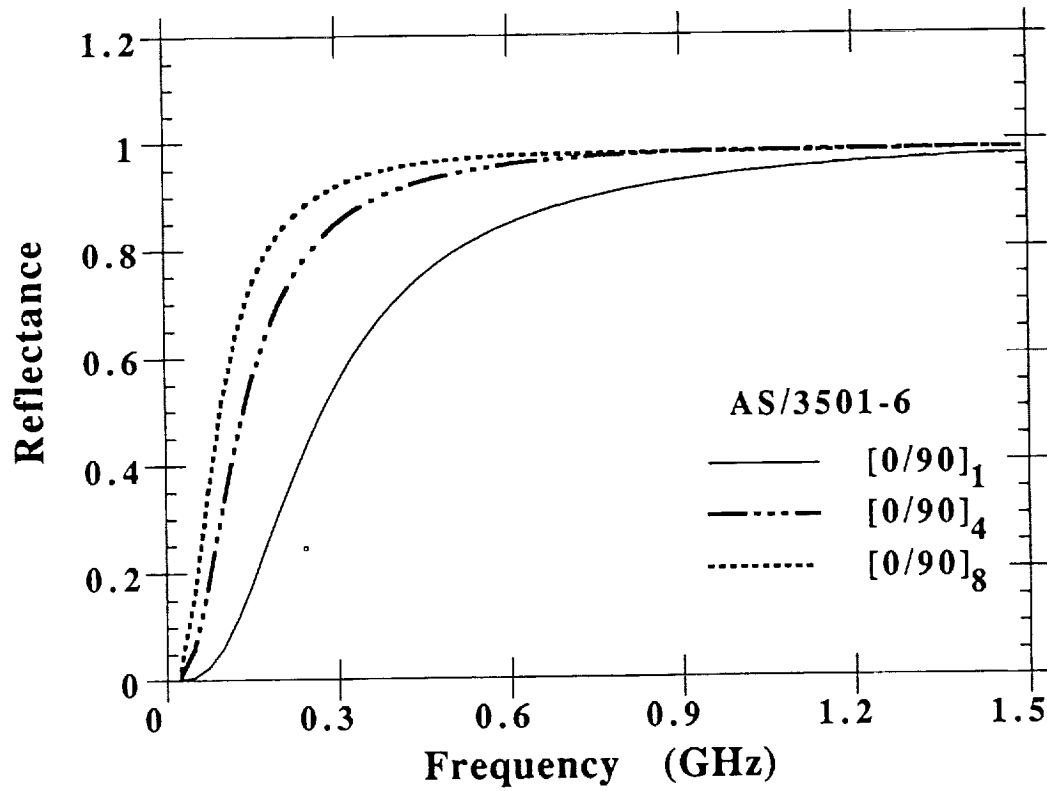


Figure 19: The reflectance of multi-layered perpendicularly crossed AS/3501-6 composite plate illuminated by an incident wave polarized at 45° with respect to the fiber orientation of the prepregs

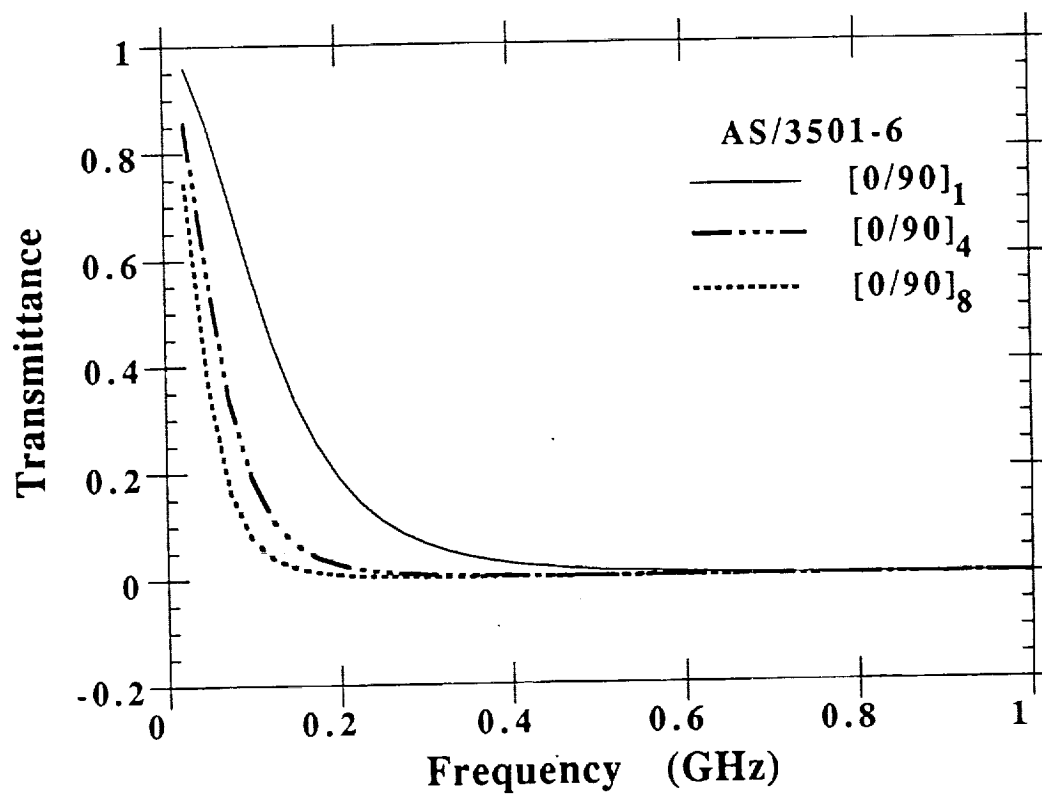


Figure 20: The transmittance of multi-layered perpendicularly crossed AS/3501-6 composite plate illuminated by an incident wave polarized at 45° with respect to the fiber orientation of the prepregs

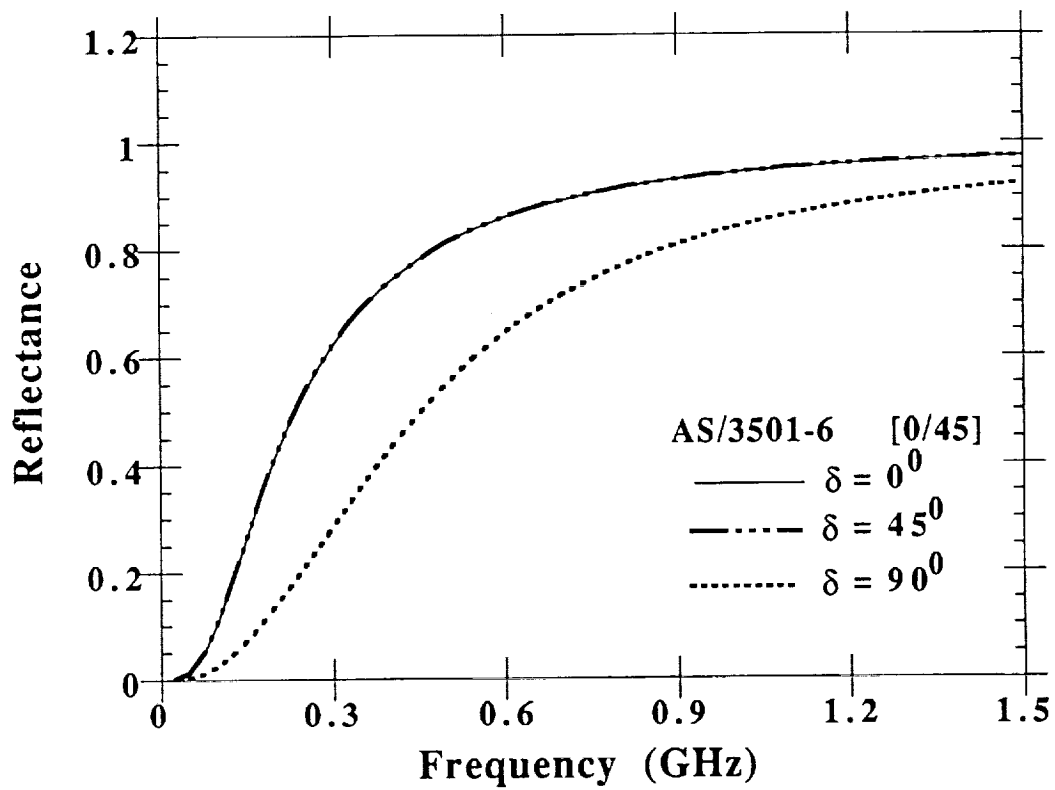


Figure 21: The reflectance of a two-ply 45° crossed AS/3501-6 composite plate illuminated by an incident wave polarized at 45° with respect to. the fiber orientation of the face prepreg

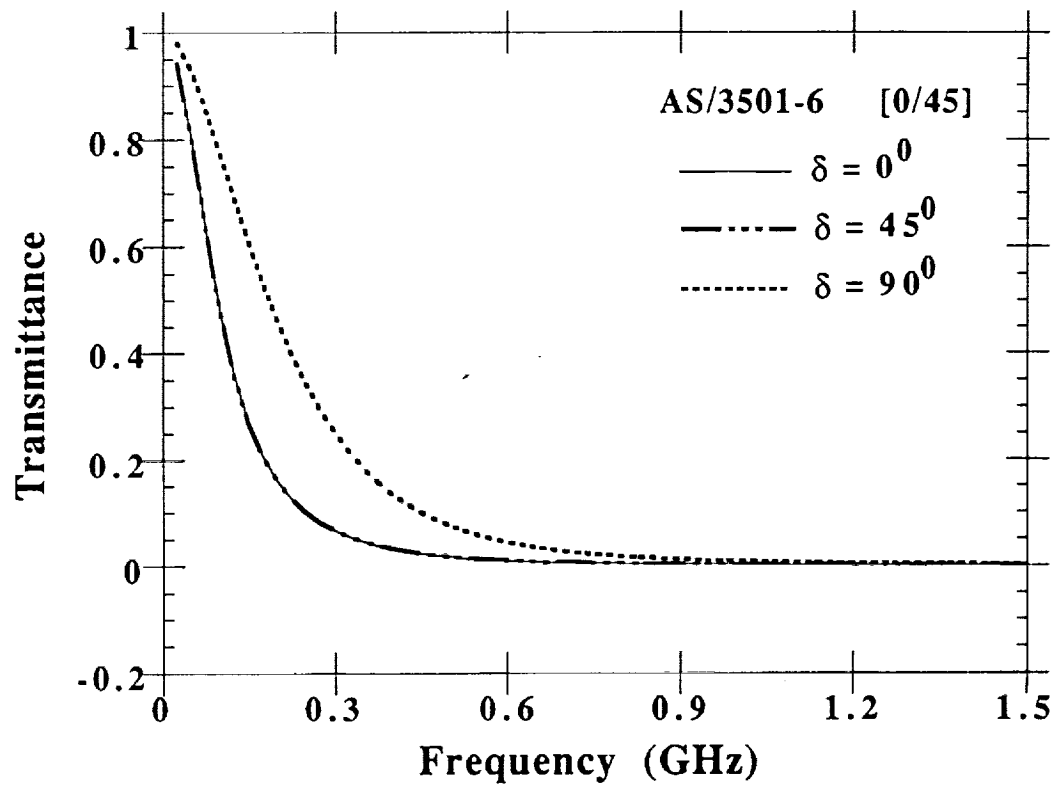


Figure 22: The transmittance of a two-ply 45° crossed AS/3501-6 composite plate illuminated by an incident wave polarized at 45° with respect to the fiber orientation of the face prepreg

III. ANTENNA TECHNOLOGY

A. Introduction

During the past quarter, significant progress in four areas of conformal antenna technology has been made. These areas are:

- a. stacked microstrip patch antennas,
- b. cavity-backed microstrip patch antennas,
- c. varactor-tuned microstrip patch antennas, and
- d. ferrite-loaded cavity-backed slot antennas.

Both microstrip and cavity-backed slot antennas are widely used at UHF and above in aerospace applications such as helicopters because they are conformal to the vehicle surface as well as light weight, low cost and easy to manufacture. The first three topics mentioned above represent novel microstrip antenna concepts that have the potential to overcome certain intrinsic disadvantages of microstrip antennas such as narrow bandwidth and the tradeoff between scan volume and bandwidth in large arrays without significantly compromising the attractive features that make microstrip antennas so desirable. In this section, progress to date in each of these areas is discussed, and plans for future work are outlined.

B. Stacked Microstrip Patch Antennas

It is well-known that a tradeoff exists between bandwidth and scan volume in a microstrip patch element phased array. The most straightforward way to improve the bandwidth of a microstrip patch antenna (for a given substrate dielectric constant) is to increase the separation between the patch and the ground plane. However, an unloaded grounded dielectric substrate supports tightly bound surface wave modes which become more strongly excited as the substrate becomes thicker. In a microstrip antenna, these surface wave modes do not contribute to main beam radiation and hence represent a loss mechanism. In a large phased array of microstrip patch elements, guided wave effects related to the surface wave modes of the unloaded substrate can lead to large mismatches (scan blindnesses) at certain scan angles. Thus,

while use of a thicker substrate results in an improvement in bandwidth, the variation in active impedance versus scan becomes more rapid. Two ways to overcome this tradeoff between scan volume and bandwidth in large arrays of microstrip elements have recently been proposed. The first is to stack the patches in two dielectric layers [6]. By stacking patch antennas, one can improve the impedance bandwidth of the antenna and/or provide for an antenna which can operate at two widely separated frequencies. The second is to break the substrate into discrete regions by placing metal walls between the patch elements [7]. The generic geometry of a stacked microstrip patch antenna is shown in Figure 23. Computer programs for the following cases of infinite arrays of probe-fed stacked patch antennas have been successfully developed and validated:

- a. one-probe-fed rectangular patches
- b. two-probe-fed rectangular patches
- c. one-probe-fed circular patches
- d. two-probe-fed circular patches

As an example of the results generated by our computer codes for infinite arrays of stacked patches, consider Figure 24. This figure illustrates broadside-matched reflection coefficient versus scan angle in both E- and H-planes for a one-probe-fed stacked rectangular patch infinite array. The polarization mismatch for the array is shown in Figure 25. The computer code required 35.2 hours of CPU time to run on a VAX 3100 workstation.

During the next quarter, additional calculated results will be generated with particular attention paid to the two-probe-fed geometries for polarization-diverse microstrip antennas. We will also begin to extend this work to the case of single stacked patch elements.

C. Cavity-Backed Microstrip Patch Antennas

Another way to overcome the tradeoff that exists between bandwidth and scan volume in a microstrip patch element phased array is to surround each patch element with a cavity. Doing so breaks the substrate into discrete regions, and prevents the excitation of surface wave modes. Recently on

a project for the Engineering Foundation, we investigated a cavity-backed patch geometry in which probe-fed circular patches are backed by rectangular cavities [7], [8]. It was demonstrated that a dramatic improvement in the scan performance of microstrip antenna phased array printed on a given substrate can be achieved by the use of a metallized cavity-backing.

It has recently been suggested that the use of circular cavities may be more appropriate due to the ease with which they may be machined [9]. In addition, the use of alternate feeding techniques such as aperture coupling is highly desirable. During the past quarter, an investigation of probe-fed circular patches backed by circular cavities was begun. We have successfully derived the dyadic Green's function for the circular cavity in the form of a discrete vector Hankel transform (DVHT) which should be the basis for development of an extremely efficient numerical code. During the next quarter, we will begin to develop numerical codes for this geometry by modifying existing codes for probe-fed circular patches backed by rectangular cavities.

D. Varactor-Tuned Microstrip Patch Antennas

Narrow bandwidth is a major disadvantage of conventional microstrip and cavity-backed slot antennas. This disadvantage precludes their use in a number of applications that could benefit from antennas possessing their many desirable characteristics. In this and the next section, we discuss some of the efforts underway to develop tunable conformal antennas. The basic concept is to start with an inherently narrow-bandwidth antenna and somehow vary one of its parameters allowing the antenna to be tuned over a fairly wide bandwidth. In many applications, it is actually more desirable to use such a tunable, inherently narrow-bandwidth antenna than an inherently wide-bandwidth antenna because of the ability of the narrow-bandwidth antenna to reject out-of-band interference.

In past quarterly reports, the basic operation of the varactor-tuned microstrip patch was explained, theoretical results for the input impedance and radiation pattern of circular patches fabricated with both silicon and GaAs varactor diodes were presented, and experimental results for the input impedance of circular patches fabricated with silicon varactor diodes were presented. During the past quarter, experimental results using GaAs varactor diodes were obtained. Figure 26 shows both measured and calculated input return loss versus frequency as a function of bias level for the GaAs

varactor-tuned patch.

Using varactor diode tuning, we have successfully designed frequency-agile microstrip patch antennas. While both silicon and GaAs diodes enable tuning of the patch frequency response, our calculations reveal that GaAs diodes are a better choice because the higher Q of the diode dramatically improves the efficiency of the antenna. Calculated minimum return loss frequencies and the antenna efficiencies (due to diode loss) at these frequencies as a function of bias level are summarized in the following table.

Varactor	Bias Level (V)	min. R. L. freq. (GHz)	efficiency (%)
Silicon	no diode	2.82	100
	20	2.66	89.6
	4	2.18	22.5
GaAs	no diode	2.82	100
	20	2.74	99.3
	4	2.52	83.2
	2	2.28	55.3

A paper [10] summarizing our work to date with varactor-tuned microstrip patches is to be presented at the upcoming IEEE Antenna and Propagation Society International Symposium in Chicago.

E. Ferrite-Controlled Cavity-Backed Slot Radiators

1. Introduction

The concept of using ferrite to magnetically tune cavity-backed slot (CBS) antennas has been around for quite some time. Previous literature, however, fails to bring to light any substantial experimental work which verifies the capabilities of such an antenna. Moreover, to the best of the authors knowledge, no analytical work has been presented which attempts to model the characteristics of a ferrite-tuned cavity radiator.

During the past quarter, a two-dimensional analytical model of a magnetically-tuneable cavity-backed slot antenna was developed with the specific intent of analyzing the scattering characteristics and the tuning capabilities of such an antenna at VHF and UHF frequencies. The work presented here, discusses the tangibility of such an antenna and brings a substantial amount of insight into the specific design qualities needed to realize these goals.

2. Background

Ferrite substrates are ferrimagnetic materials constructed from solid ceramic materials which have been sintered with certain metal oxides at high temperatures. At microwave frequencies they exhibit strong magnetic effects, which result in anisotropic behavior. By applying an external DC magnetic field, the permeability tensor of the ferrite is altered, and thus the electrical characteristics of the ferrite substrates used in the CBS structure are varied. Because of this, the antenna will resonate at different frequencies for different values of the applied DC magnetic field.

There are two types of modes that can be excited inside the cavity. The first type of mode is the dynamic mode, which depends mainly on the dielectric properties of the materials inside the cavity, including dielectric constants of these materials and their relative permeabilities. The second type of mode is the magnetostatic mode. For magnetostatic modes, the permeability tensor gives rise to low frequency magnetostatic volume-wave modes, which become appreciable with large external biases. It is these volume wave modes that allow a microwave CBS antenna to operate in a frequency range lower than those of the dynamic mode.

3. Two-dimensional analytical model

The analysis presented in this report utilizes a spectral domain admittance Green's function in conjunction with the transmission matrix method to account for multiple substrate layers within the cavity. In this method, closed form expressions of the Green's function are derived for the regions above and within the cavity, and take into account the anisotropic characteristics of the ferrite. The full-wave formulation uses the physical equivalence principle, along with Galerkin's procedure, to obtain the scattered fields produced by the antenna when the structure is excited by an incident plane wave. Figure 27 shows the schematic diagram of a multiple-layered cavity filled with both dielectric and ferrite materials. Tuning capabilities of both magnetostatic and dynamic modes were analyzed for a variety of layering configurations and different cavity dimensions. The results presented here examine several antenna characteristics which may have an appreciable effect on the performance of the antenna and its tuning capabilities.

4. Dielectric-loaded cavities vs. ferrite-filled cavities

In order to design a physically realizable magnetically-tunable CBS antenna, the primary question that needs to be addressed is: What effect does the ferrite have on the cavity-backing which will allow for tuning capabilities, and what characteristics will allow it to operate at lower frequencies? In order to answer this question, we examine two cases. The first case is a 2D rectangular cavity-backed slot in an infinite ground plane partially filled with a dielectric substrate. The second case is developed by replacing the dielectric with a ferrite substrate of the same relative dielectric constant.

If we illuminate the CBS structure by an incident plane wave with hard polarization (TM_z), we obtain the resulting scattering width of the antenna as a function of frequency given in Figure 28. The peaks in the figure represent the modes at which the antenna will resonate.

It is evident from the figure that by replacing the dielectric with a ferrite substrate, the resonant frequency of the dominant dynamic mode of the structure has been shifted as a result of the alteration of the electrical dimensions of the cavity. Even more interesting, is the presence of a weak magnetostatic volume-wave mode at approximately 60 MHz for $H_0=0$ Oersted. The presence of this mode coincides with the findings of the classic

papers by others on the propagation of volume-wave magnetostatic modes in ferrite substrates. We can see from the figure, however, that without an external bias, this mode is far too weak to be considered as a useable resonant mode.

In order to utilize these volume-wave modes as a source of radiation, it is necessary to apply a substantial DC magnetic field to the ferrite substrates. By increasing the magnetic bias, the magnetostatic modes become gradually stronger in magnitude and shift over in frequency as well. Figure 28 shows the results of the scattering width of the antenna as the external bias is increased from 0.0 Oersted to 300.0 Oersted. As shown in the graph, the volume-wave modes tune over a substantial frequency range whereas the dynamic mode is less affected by the magnetic bias. The following table shows the magnitudes and resonant frequencies of the magnetostatic volume-wave modes as the external bias is increased.

DC Bias (Oersted)	Frequency (GHZ)	Scattering Width (dB/m)
0.0000	0.2007	-26.73
100.00	0.7570	-8.56
300.00	1.399	-5.42

5. Design considerations

5.a. Airgap and low dielectric material effects In previous work on ferrite antennas, there were no air gaps between radiating elements (such as slots, microstrip patches, etc.) and ferrite layers. Also, the ferrite has always been metal backed, i.e. there was no separation between the ferrite substrate and the ground plane. Clearly, losses in ferrite will have a significant impact on the total antenna efficiency if there is no separation between the radiating elements and the ferrite. Also, ground plane has the effect of attenuating volume wave modes and therefore, there has to be a separation between ferrite and ground plane to support low loss volume waves.

First, we consider the effects of increasing the airgap between the slot and ferrite in order to increase the antenna efficiency. To investigate such effects, the thickness of the ferrite and the low dielectric substrate at the bottom of the cavity were assumed constant and the airgap is varied. The analysis shows that the scattering width of the volume-wave modes increases as the air gap increases, as shown in Figure 29. Increasing the air gap also resulted in increasing the bandwidth of both the magnetostatic and dynamic modes of the cavity.

Secondly, we study the effect of placing a low dielectric substrate at the bottom of the cavity to shield the ferrite from the ground plane. From Figure 30, it is evident that an increase in the ground layer will increase the scattering width of the magnetostatic modes of the antenna by approximately 1.0 dB. From these results, we conclude that the inclusion of a sufficient airgap and a low dielectric grounding layer will add approximately 4 dB to the scattering width of volume-wave modes.

5.b. Effect of cavity width It is well known that the cavity dimensions will have a drastic effect on the dynamic resonant modes of the CBS antenna. It is not well known, however, what effect these dimensions will have on the magnetostatic resonant modes of the ferrite-loaded cavity antenna. From the 2D analytical model, we can show that an increase in the cavity dimensions along the direction of magnetization will in fact greatly increase the magnitude of the ferrite modes as well as shift them toward lower frequencies of resonance.

Figure 31 shows the results of the scattering width of the antenna as the cavity width is varied from 0.6 inches to 2.0 inches. As the figure shows, an increase in the cavity width has a large impact on the magnitude of the magnetostatic mode but not on the dynamic mode of the cavity. The following table shows the actual increases in the magnitudes of the lowest order volume-wave mode and the associated frequency shift.

Cavity Width (inches)	Frequency (GHZ)	Scattering Width (dB/m)
0.6	0.8013	-11.88
1.0	0.7520	-8.25
2.0	0.6286	-4.78

5.c. Effect of the slot width The width of the slot is yet another cavity dimension that can be considered in the design of a CBS antenna. An increase in the slot dimension may greatly increase the bandwidth of the dynamic resonant mode, but efficiency is reduced as a result. The magnitude of the magnetostatic mode, on the other hand, is not significantly altered, but does cause a slight shift in the frequency of resonance, as shown in Figure 32. This shift will only become appreciable for large cavity dimensions, where the slot width is allowed to vary over a significant range.

F. Future Work

We are in the process of building an optimized magnetostatic volume wave antenna. We acquired strong permanent magnet tips to provide the required magnetization for the ferrite layers. Other materials, needed to build the antenna, are already available to us. We intend to extend our analysis to include the three dimensional case and evaluate the difference between the two dimensional and the three dimensional theories.

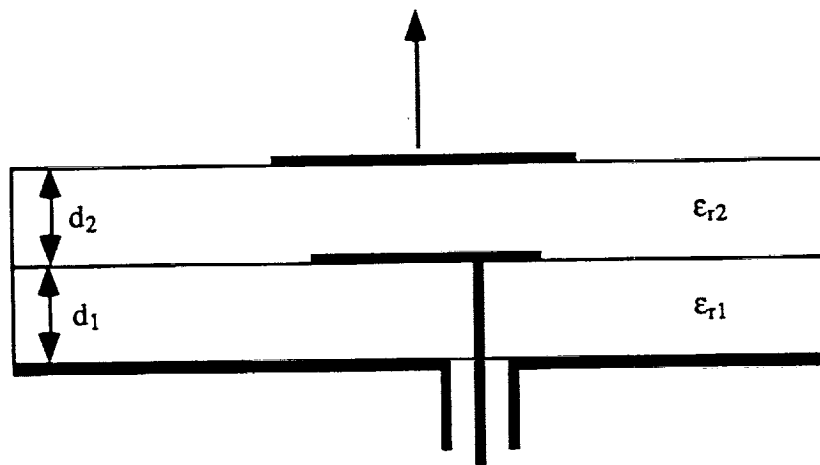


Figure 23: Geometry of a stacked patch phased array. The bottom patch is probe-fed via the center conductor of a coaxial connector, and the top patch is parasitic.

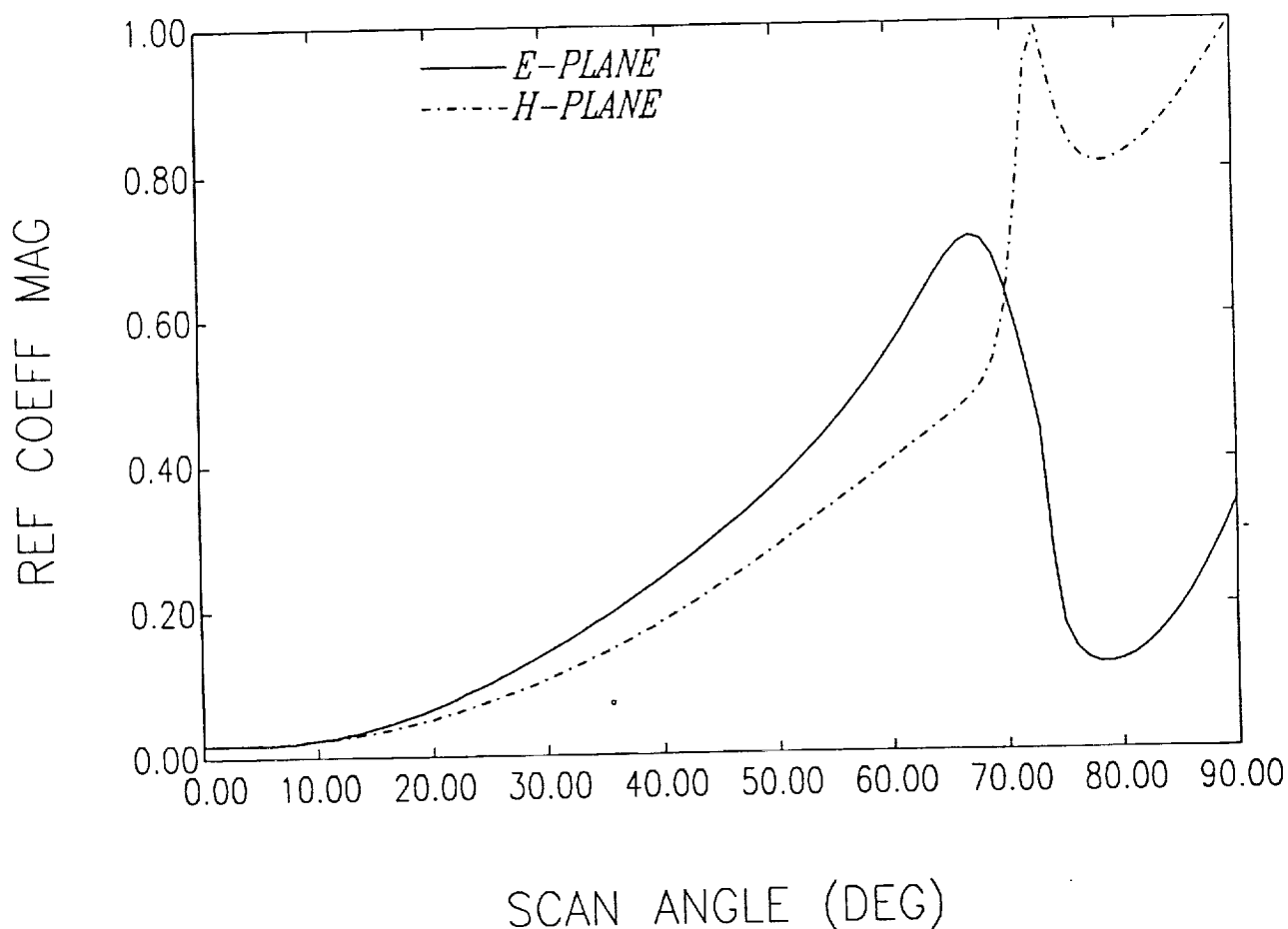


Figure 24: Broadside-matched reflection coefficient magnitude versus scan angle for an infinite array of stacked one-probe-fed rectangular microstrip patches. The substrate parameters of this array are:

$\epsilon_r = 2.5$, $d_1 = 0.051\lambda_0$, $\epsilon_r = 1.5$, $d_2 = 0.051\lambda_0$, where λ_0 is the free-space wavelength. The lower patch is $0.29\lambda_0$ by $0.29\lambda_0$; the upper patch is $0.285\lambda_0$ by $0.285\lambda_0$. The lower patch is fed by a probe feed of radius $0.01450\lambda_0$ at a point $0.0725\lambda_0$ from the center along the x-axis. The element spacing in the x-direction is $0.51\lambda_0$; the element spacing in the y-direction is $0.5\lambda_0$.

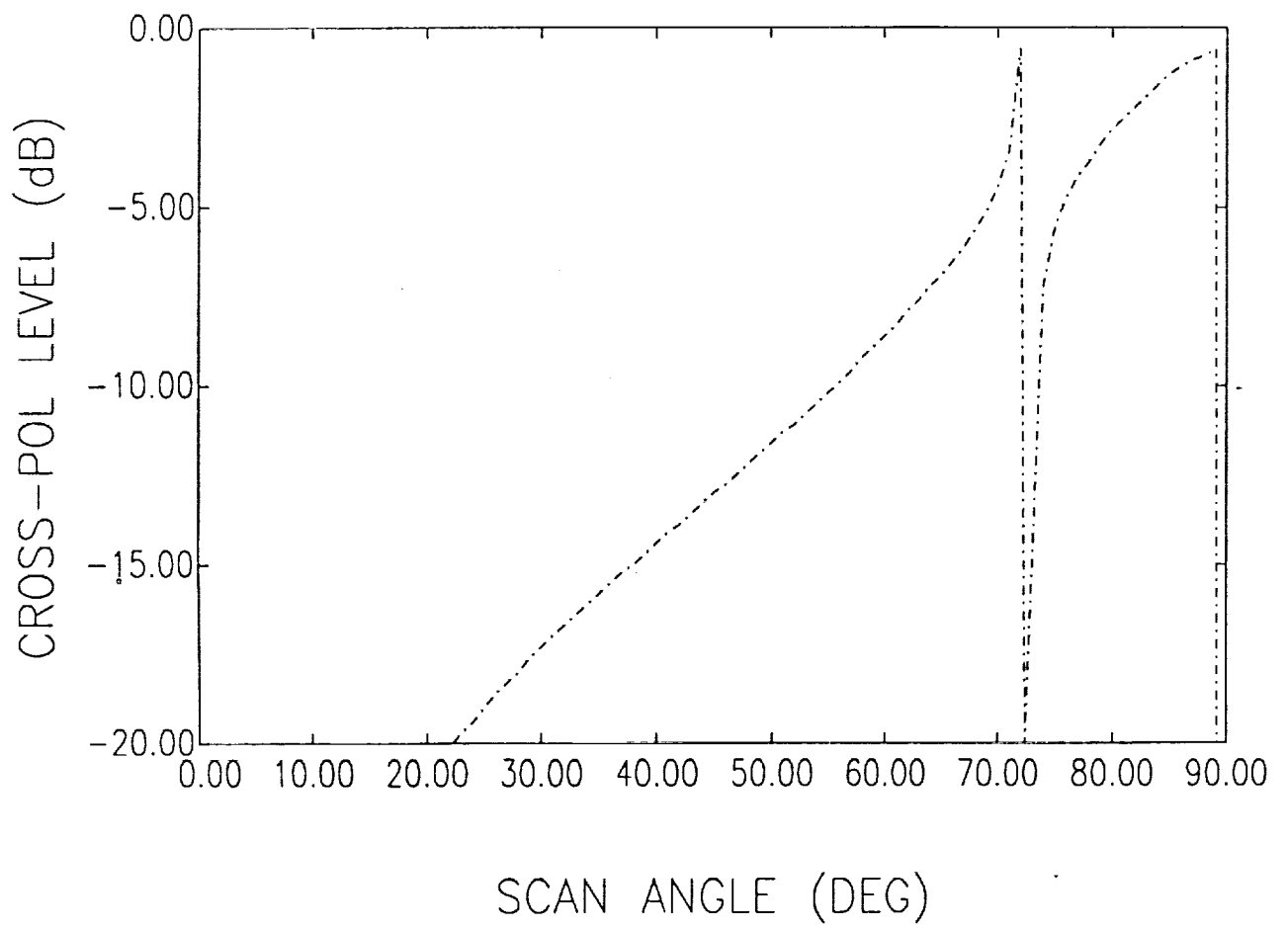


Figure 25: H-plane polarization mismatch for the array shown in the previous figure

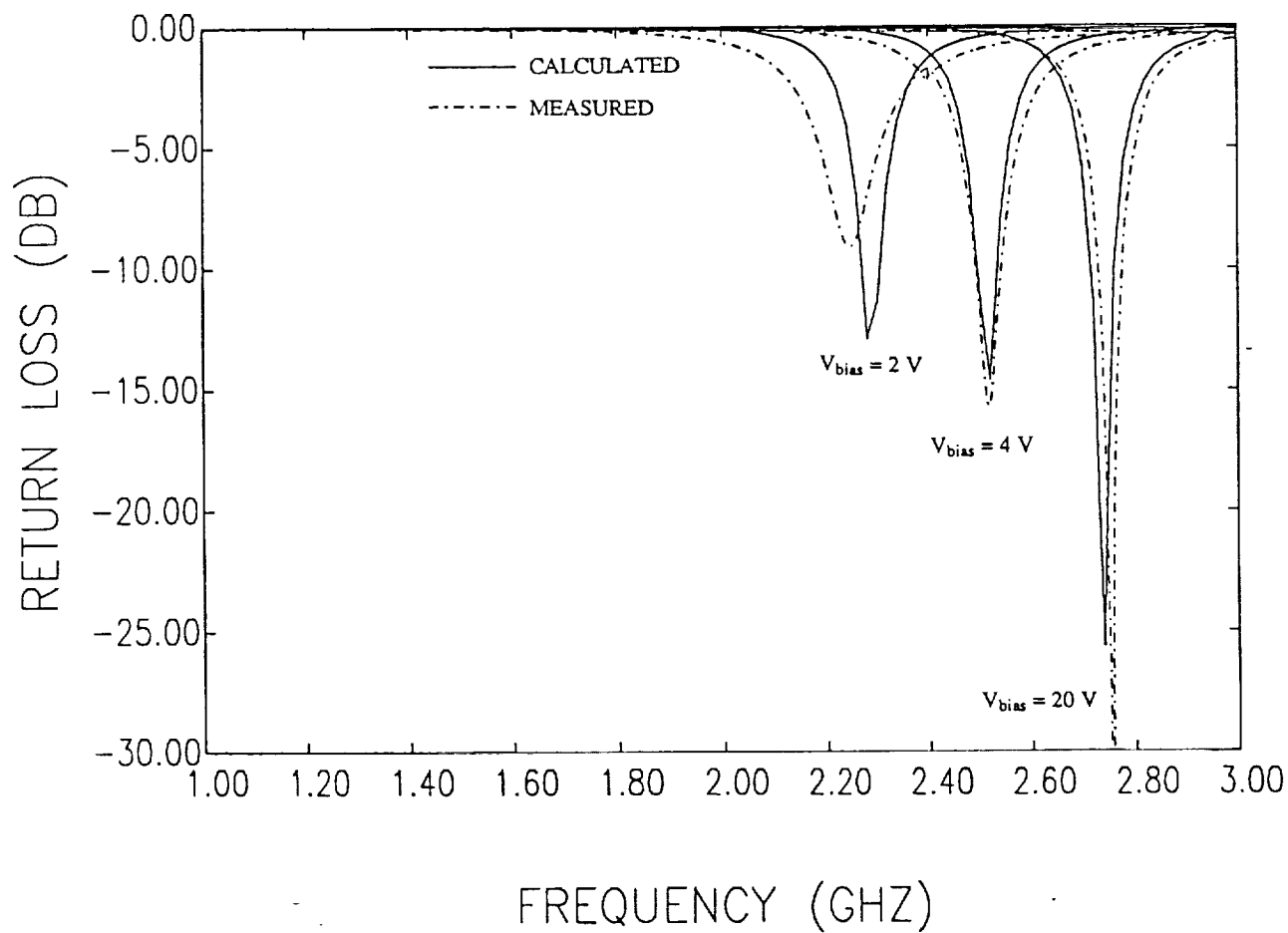


Figure 26: Measured and calculated input return loss of the GaAs varactor-tuned microstrip patch antenna for bias voltages of 20, 4 and 2 volts.

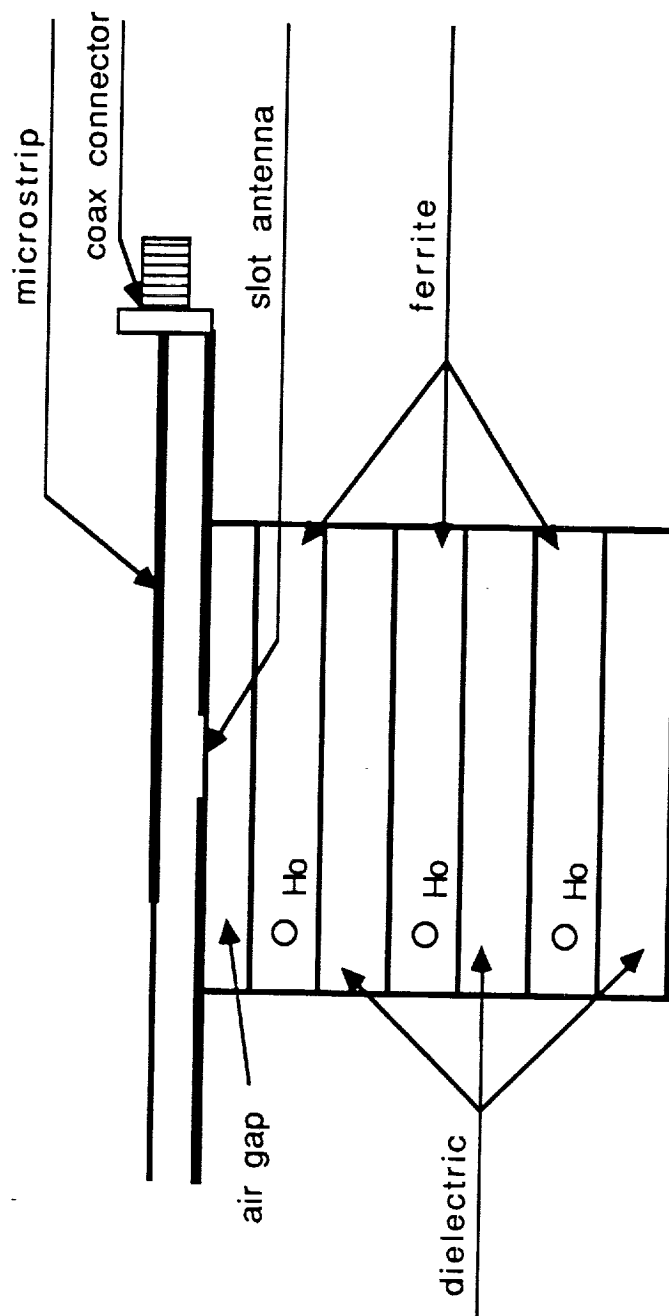


Figure 27: Schematic diagram of a multiple-layered cavity filled with both dielectric and ferrite materials.

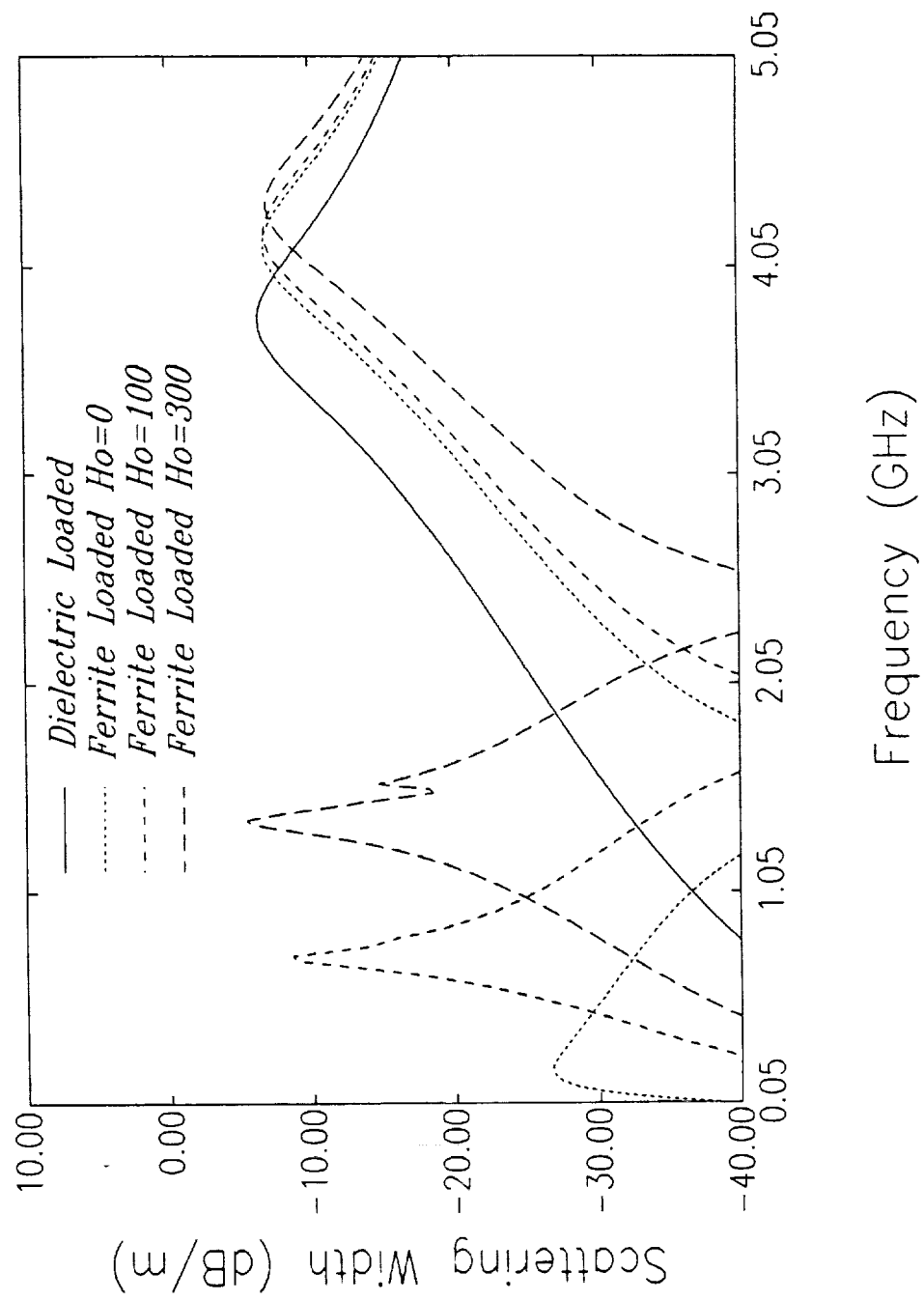


Figure 28: Scattering width of a CBS antenna versus frequency.

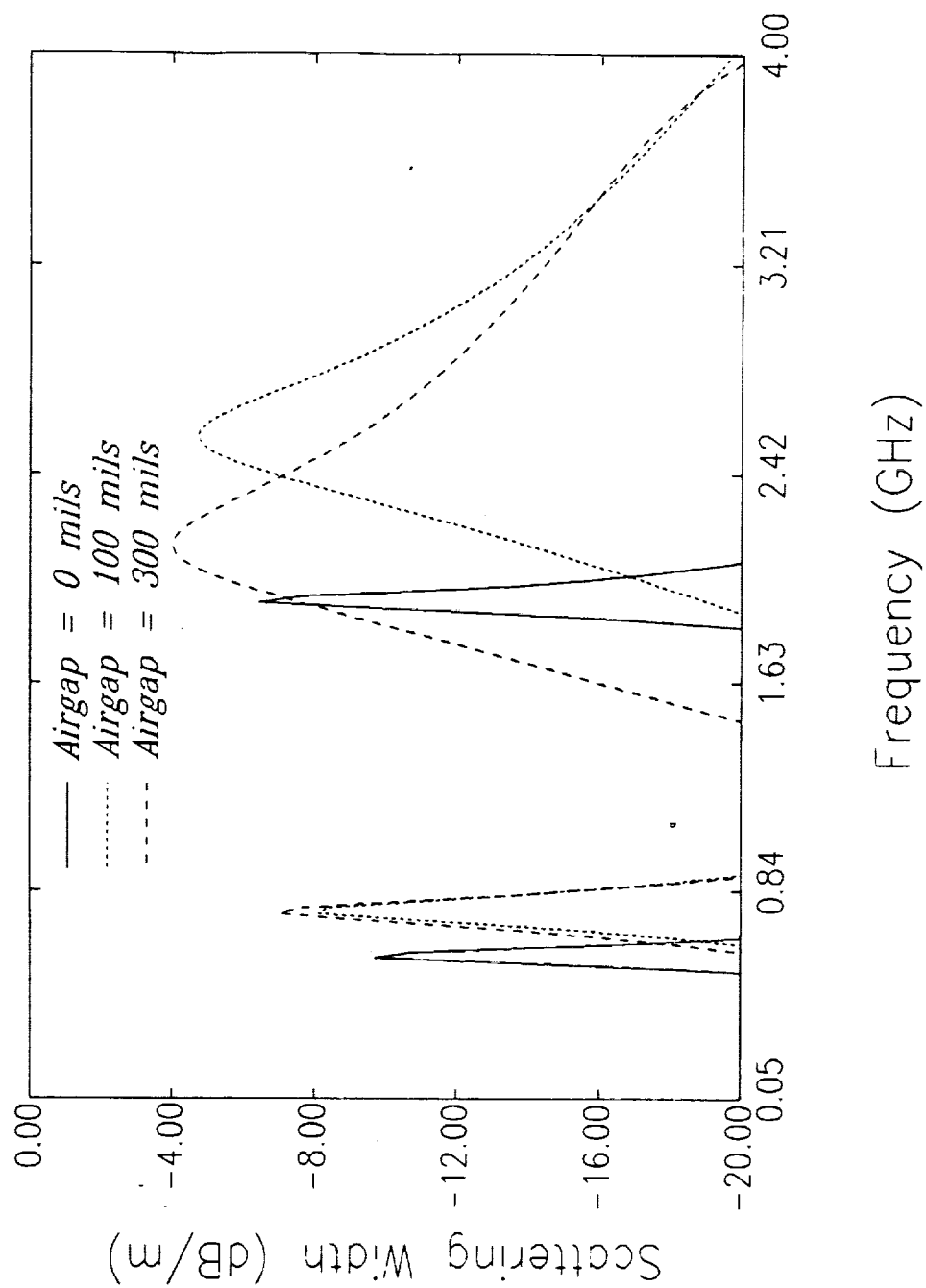


Figure 29: Scattering width of the volume-wave modes versus frequency and air gap.

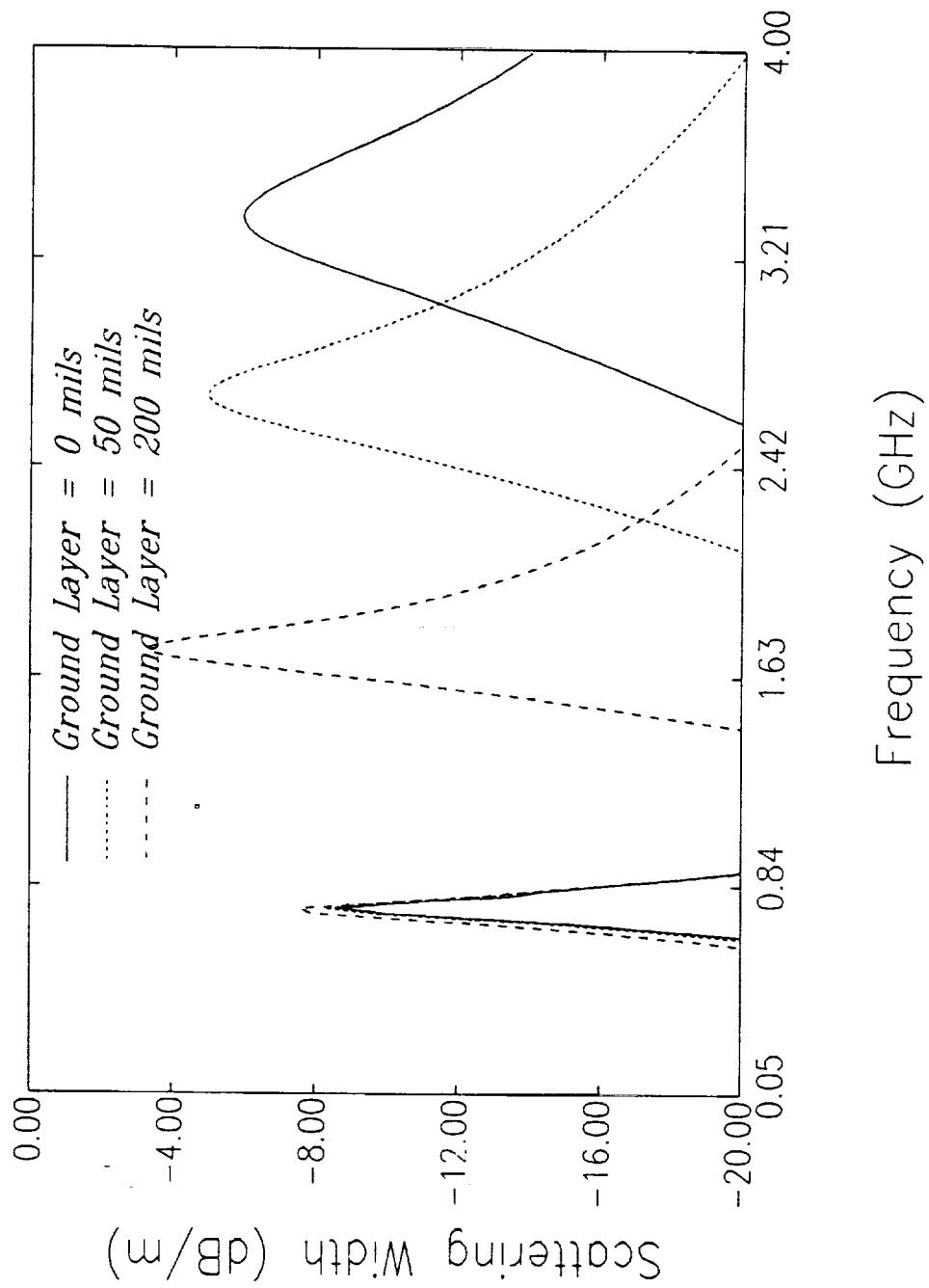


Figure 30: Scattering width of a CBS antenna with ground layer.

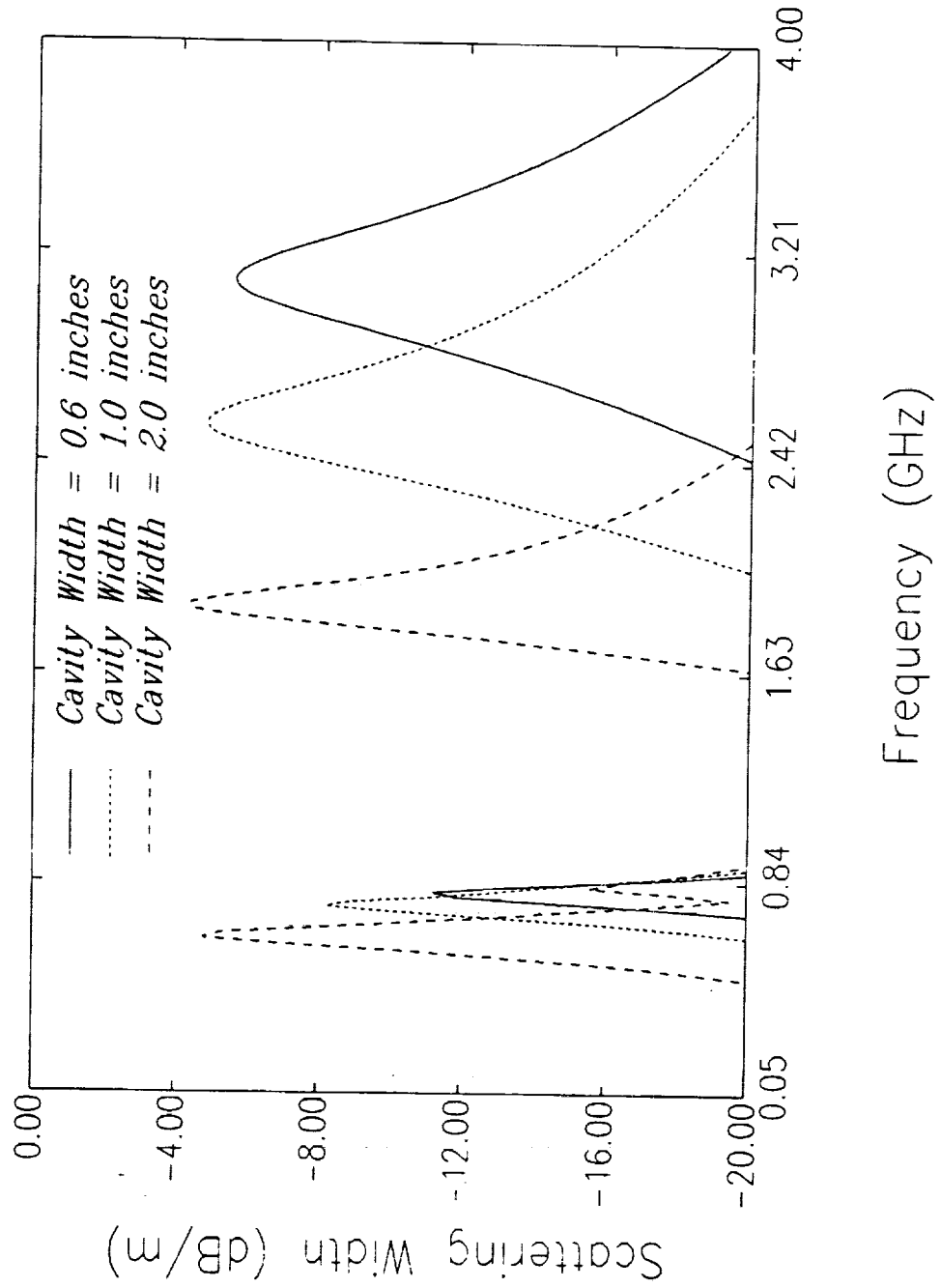


Figure 31: Scattering width of a CBS antenna versus the cavity width and frequency.

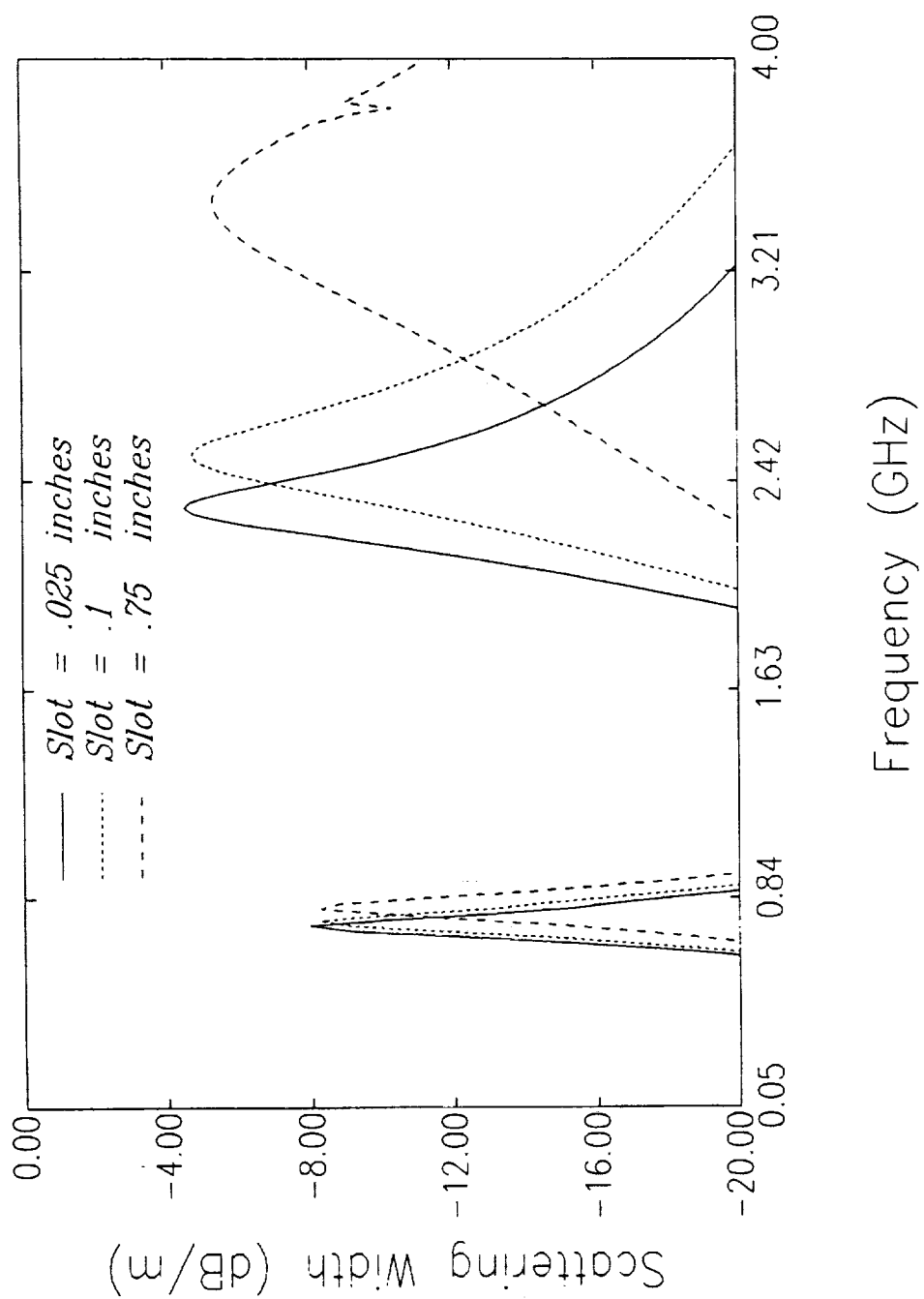


Figure 32: Scattering width of a CBS antenna versus frequency and the slot width.

References

- [1] Woo Il Lee and G. S. Springer, "Interaction of Electromagnetic Radiation with Organic Matrix Composites," *J. of Composite Materials*, Vol. 18, P. 357, July, 1984
- [2] Woo Il Lee and G. S. Springer, "Microwave Curing of Composites," *Journal of Composite Materials*, Vol. 18, P. 357, July, 1984
- [3] M. A. Morgan, D. L. Fisher and E. A. Milne, "Electromagnetic Scattering by Stratified Inhomogeneous Anisotropic Media," *IEEE Transaction on Antennas and Propagation*, Vol. Ap-35, No.2, P.191, Feb., 1987
- [4] V. Volpe, "Estimation of Electrical Conductivity and Electromagnetic Shielding Characteristics of Graphite/Epoxy Laminates," *J. of Composite Materials*, Vol. 14, P. 189, July, 1980
- [5] O. Hashimoto and Y. Shimizu, "Reflecting Characteristics of Anisotropic Rubber Sheets and Measurement of Complex Permittivity Tensor," *IEEE Transactions on Microwave Theory and Techniques*, Vol. MTT-34, No.11, P. 1202, Nov., 1986
- [6] Y. Lubin and A. Hessel, "Wide-band, wide-angle microstrip stacked-patch-element phased arrays," *IEEE Trans. Antennas and Propagation*, Vol. 39, no. 8, pp. 1062-1070, Aug. 1991.
- [7] J.T. Aberle, "On the use of metallized cavities backing microstrip antennas," in *IEEE Antennas and Propagation Soc. Int. Symposium Digest*, 1991, pp. 60-63.
- [8] J.T. Aberle, "Novel microstrip antenna configurations for enhanced performance," Final Report, Air Force Engineering Foundation Grant RI-B-90-19, Sept. 1, 1991.
- [9] J.A. Navarro, K. Chang, J. Tolleson, S. Sanzgiri, R.Q. Lee, "A 29.3 GHz Cavity-Enclosed Aperture-Coupled Antenna for Microwave Circuit Integration," *IEEE Microwave and Guided Wave Letters*, Vol. 1, no. 7, pp. 170-171, Jul. 1991.

- [10] J.T. Aberle, M. Chu, C.R. Birtcher, "Scattering and radiation properties of varactor-tuned microstrip antennas," accepted for presentation at the 1992 IEEE Antenna and Propagation Society International Symposium.